1   **REVISION 2**

2   Tracking dynamic hydrothermal processes: Textures, *in-situ* Sr-Nd

3   isotopes and trace element analysis of scheelite from the Yangjiashan

4   vein-type W deposit, South China

5   WEI LI[1], GUIQING XIE[2*], NIGEL J. COOK[3], JINGWEN MAO[1,2], CHAO LI[4], CRISTIANA L.

6   CIOBANU[5], ZHIYUAN ZHANG[6]

7   [1]*Ministry of Natural Resources (MNR) Key Laboratory of Metallogeny and Mineral*

8   *Assessment, Institute of Mineral Resources, Chinese Academy of Geological Sciences*

9   *(CAGS), Beijing 100037, China*

10   [2]*Institute of Earth Sciences, China University of Geosciences, Beijing 100083, China*

11   [3]*School of Civil, Environmental and Mining Engineering, The University of Adelaide,*

12   *Adelaide, SA 5005, Australia*

13   [4]*National Research Center for Geoanalysis, Beijing 100037, China*

14   [5]*School of Chemical Engineering and Advanced Materials, The University of*

15   *Adelaide, Adelaide, SA 5005, Australia*

16   [6]*Hebei GEO University, Shijiazhuang 050031, China*

[*] Corresponding author E-mail address: xieguiqing@cugb.edu.cn

ABSTRACT

17

18   Texturally complex minerals can provide critical information on dynamic hydrothermal processes.

19   This study combines cathodoluminescence (CL), laser ablation-inductively coupled plasma mass

20   spectrometry (LA–ICP–MS), and high-resolution femtosecond laser ablation multi-collector

21   inductively coupled plasma mass spectrometry (fs–LA–MC–ICP–MS) analyses, to document

22   textures, *in-situ* Sr-Nd isotope systematics, and trace element compositions of texturally-complex

23   scheelite from the Yangjiashan W deposit, South China. The major motivation for this contribution

24   was to reveal the correlation between CL response, textures, and trace element concentrations;

25   document the origin of various REE fractionation patterns; and to characterize grain scale *in-situ*

26   variability of Sr-Nd isotopes of scheelite.

27   Five sub-types of scheelite from both stages, including Sch1 and Sch2 from Stage 1, and Sch3 to

28   Sch5 from Stage 2, are identified. CL images feature complex oscillatory, patchy, and evidence for

29   coupled dissolution-reprecipitation reaction. These scheelites precipitated from reduced fluids and

30   are close to endmember in composition, with Mo concentrations below 46 ppm. Concentrations of

31   other elements vary: Sr (36-1,025 ppm); Nd (8-351 ppm); and Na (7-300 ppm). LA–ICP–MS

32   element maps reveal a large variability in REE concentrations among oscillatory zones, and no

33   consistent behavior between REE, Sr and Mo concentration, and CL intensity. Four distinct

34   chondrite-normalized REE fractionation patterns are recognized: LREE-enriched, MREE-enriched,

35   HREE-enriched, and flat patterns. Complex Eu anomalies (δEu = 0.2 to 20.7) are recognized among

36   the five sub-types and are commonly observed within individual grains. Fluid compositions,

37   different substitution mechanisms (i.e., $Ca^{2+} + W^{6+} = REE^{3+} + Nb^{5+}$, and $2Ca^{2+} = REE^{3+} + Na^{+}$,

38      $3Ca^{2+} = 2REE^{3+} + \square Ca$, where $\square Ca$ is a Ca-site vacancy), primary-secondary processes (i.e.,

39   oscillatory and dissolution-reprecipitation, respectively), all contribute to the variation in REE

40   fractionation patterns. Local fluctuation in fluid pH is responsible for the complex Eu anomalies.

41   *In-situ* Sr and Nd isotope signatures for the five sub-types of scheelite show relatively large ranges,

42   i.e., the initial $^{87}Sr/^{86}Sr$ ratios range from 0.71336 to 0.72617, and the initial εNd values ranging

43   from -24.9 to -7.7, suggesting a source derived from a mixture of magmatic-hydrothermal fluids

44   and the Neoproterozoic slate. Decreasing $^{87}Sr/^{86}Sr$ ratios from Sch2 to Sch5 record decreasing

45   fluid-rock interaction intensity. Large variation of εNd(t) values (-24.9 to -7.7) of scheelite with

46   oscillatory zoning textures may relate to changes of Sm/Nd ratio of scheelite and contamination

47   from wall rock with inhomogeneous Nd isotope composition. This study highlights the importance

48   of performing coupled LA–ICP–MS mapping and *in-situ* Sr-Nd isotope analyses on sample material

49   that has been characterized in detail at the micron-scale.

50   **Keywords:** Scheelite, REE fractionation patterns, *in-situ* Sr-Nd isotope analysis, tungsten deposits,

51   Yangjiashan

52   **INTRODUCTION**

53   Appreciating the complexity of hydrothermal processes is critical for accurately constraining the

54   genesis of ore deposits (e.g., Robb 2005). Veins composed of hydrothermal minerals contain

55   integrated information about the hydrothermal fluids, including composition and their migration

56   path through the Earth's crust. Minerals displaying growth or compositional zoning, such as

57   scheelite, quartz, and sulfides precipitated from hydrothermal fluid, can express the evolution of

58   hydrothermal fluid (Loomis 1983; Shore and Fowler 1996; Brugger et al. 2000; Rusk and Reed

59   2002; Cook et al. 2009; Barker and Cox 2011). Mineralogical studies bridging nano- to macroscales

60   of observation can thus provide critical information on the ore-forming processes (Cook et al. 2013,

3

61 2017; Ciobanu et al. 2016; Fougerouse et al. 2016; Li et al. 2019).

62   Scheelite, one of the most economically important tungsten minerals, has been widely used to

63 decipher ore-forming processes and sources of fluids and metals (Ghaderi et al. 1999; Brugger et al.

64 2000, 2002; Poulin et al. 2018; Scanlan et al. 2018; Sciuba et al. 2020). Studies have revealed that

65 scheelite, particularly from magmatic-hydrothermal deposits (e.g., skarns), are commonly

66 heterogeneous with respect to textures (e.g., pronounced oscillatory zonation and

67 dissolution-reprecipitation textures) and trace element distributions at the grain-scale (Song et al.

68 2014; Poulin et al. 2016, 2018; Sun and Chen 2017; Zhao et al. 2018). Such phenomena carry

69 inference for the interpretation of rare earth element (REE) distribution patterns and isotope

70 systematics (e.g., Sr) which have been proposed as valuable interpretive tools (Brugger et al. 2000,

71 2002). Despite this, few studies have clearly illustrated the relationships among trace element

72 distributions at the scale of single grains, or between the concentrations of REE (or other trace

73 elements) and the CL response (Poulin et al. 2016; Su et al. 2019).

74   Scheelite can accommodate measurable amounts of Sm, Nd, and Sr, but negligible Rb (Bell et al.

75 1989; Kempe et al. 2001). Radiogenic ^{87}Sr produced from ^{87}Rb decay is thus insignificant in

76 scheelite, enabling initial ^{87}Sr/^{86}Sr ratios to be preserved (Bell et al. 1989). Considering the

77 grain-scale variability of Sm/Nd ratios due to the heterogeneity in texture and corresponding REE

78 concentrations, together with the progressive fluid-rock interaction which is critical for the

79 formation of tungsten deposits (Wood and Samson 2000; Lecumberri-Sanchez et al. 2017), the Sr

80 and Nd isotope composition of ore-forming fluid will evolve in both time and space, and therefore,

81 any small-scale compositional heterogeneity in scheelite may also be reflected by varying Sr-Nd

82 isotope values (Brugger et al. 2002; Kozlik et al. 2016; Scanlan et al. 2018; Song et al. 2019). For

83 example, different initial ^{87}Sr/^{86}Sr values and εNd(t) values were documented among distinct

4

84   micro-drilled scheelite separates from a single large crystal with different REE patterns from

85   quartz-vein gold deposits (Brugger et al. 2002). It is, however, unclear thus far to what extent the

86   large variation and overlap in the Sr-Nd isotope data for scheelite displaying heterogeneous textures

87   may be masked by conventional bulk powder chemistry. This observation highlights the necessity

88   of *in-situ* analyses of coupled Sr-Nd isotope measurements on fully characterized samples in any

89   attempt to better understand the source of metals and dynamic ore-forming processes.

90   The present study focuses on the Yangjiashan scheelite-quartz vein deposit, a representative

91   tungsten deposit of Paleozoic age in South China (Xie et al. 2019a). We characterize scheelite

92   textures and chemistry, involving specific CL responses and corresponding trace element analyses,

93   including both spot data and element maps determined by laser ablation-inductively coupled plasma

94   mass spectrometry (LA–ICP–MS), coupled with Sr-Nd isotopes analyses determined *in-situ* by

95   femtosecond laser ablation multi-collector inductively coupled plasma mass spectrometry (fs–LA–

96   MC–ICP–MS). We aim to advance understanding of the grain scale *in-situ* variability of trace

97   element and Sr-Nd isotope distributions in scheelite, thus highlighting the necessity of *in-situ*

98   analyses of scheelite for correct interpretation of ore-forming processes.

GEOLOGICAL BACKGROUND

100   The Xiangzhong Sb–Au metallogenic province is located in the southeastern part of the Yangtze

101   Block, South China (Fig. 1a). This province hosts a large concentration of Sb–Au deposits (Hu et al.

102   2017; Li et al. 2019), including the world-class Xikuangshan Sb deposit, and the Gutaishan and

103   Longshan Au–Sb deposits (Fig. 1b). In addition, two styles of economic tungsten deposits have

104   been discovered and mined, including quartz veins and skarns (Fig. 1b). Quartz vein mineralization

105   is represented by the Yangjiashan scheelite-quartz deposit (Xie et al. 2019a), the Woxi Au–Sb–

5

scheelite-wolframite-quartz deposit (Zhu and Peng 2015), and the Shaxi scheelite-wolframite-quartz

deposit (Su et al. 2016). Tungsten skarns include Caojiaba and Darongxi (Xie et al. 2019b; Zhang et

al. 2020).

The Yangjiashan deposit is located at the contact zone between Neoproterozoic rocks and the

Baimashan granite (Fig. 2) and has a total WO_3 resource of ~39,000 metric tonnes at an average

grade of 0.70% WO_3 (Xie et al. 2019a). Deposit geology has been described by Xie et al. (2019a)

and is briefly summarized here. The scheelite-quartz veins are dominantly hosted in psammitic slate

of the Mobin Formation, a unit that belongs to the Neoproterozoic Banxi Group (Fig. 2). Intrusions

in the Yangjiashan orefield are predominantly by biotite monzogranite (Fig. 2) and represent the

northernmost part of the Baimashan pluton (Fig. 1b). SHRIMP U–Pb zircon methods yield an

intrusion age of 407 ± 3 Ma, coeval with the Re-Os age of hydrothermal molybdenite (404 ± 3 Ma)

intergrown with scheelite (Xie et al. 2019a). Coupled stable isotope compositions, including

$\delta^{18}O_{H2O}$ and δD values for quartz (-1.2 to +3.4‰ and -87 to -68‰, respectively), and $\delta^{34}S$ values of

sulfides (-2.9 to -0.7‰), all support a magmatic-hydrothermal fluid source mixed with meteoric

water for the Yangjiashan deposit (Xie et al. 2019a).

Two stages of scheelite mineralization are identified (Xie et al. 2019a): early greisen (Stage 1)

and late quartz veins (Stage 2) (Fig. 3); the latter represents the major ore type. Greisen ores are

composed of quartz, muscovite, scheelite, and arsenopyrite (Fig. 4a, b). The quartz vein-type ores

consist of quartz, scheelite, arsenopyrite, chalcopyrite, pyrite, and minor fluorite, cassiterite, and

muscovite (Fig. 4c–i). Scheelite grains from both stages occur commonly as cm-sized aggregates

with pinkish to whitish color. Mineral assemblages comprising native bismuth and pyrrhotite within

quartz veins, and the presence of CH_4 in fluid inclusions hosted within quartz and scheelite (Xie et

al. 2019a), suggest scheelite precipitation from relatively reduced fluids in both stages.

6

129   SAMPLING AND ANALYTICAL METHODS

130   A suite of scheelite-bearing samples collected from different mining adit levels, representing

131   both stages of mineralization (Fig. 4), were selected for cathodoluminescence (CL) imaging of

132   grain-scale features, measurement of trace element distributions, and *in-situ* Sr-Nd isotope analyses.

133   Two samples (YJS-69 and YJS-87; Fig. 4a, b) are from Stage 1, and seven samples (YJS-36,

134   YJS-39, YJS-55, YJS-62, YJS-66, YJS-67, and YJS-71; Fig. 4c–i) are from Stage 2. Detailed

135   characteristics of these samples are described in Supplemental[1] Table S1. Each sample was mounted

136   in epoxy and prepared as a one-inch-diameter polished block.

137   Scheelite CL images were generated using a FEI Quanta 600 (MLA) with EDX and Gatan CL

138   detectors (Adelaide Microscopy, The University of Adelaide). All measurements were performed at

139   an accelerating voltage of 25 kV and a beam current of ~3 nA.

140   *In-situ* LA–ICP–MS trace element spot analysis and mapping of scheelite were obtained using

141   a 213 nm, Q-switched, Nd: YAG New Wave UP 213 laser ablation system, coupled to an Agilent

142   7900 Quadrupole ICP–MS instrument (Adelaide Microscopy, The University of Adelaide). Data

143   were processed with Iolite using ^{44}Ca as the internal standard. Operating conditions, isotopes

144   measured, and data processing methodologies are given in Supplemental[1], and average minimum

145   detection limits and dwell times are given in Supplemental[1] Table S2.

146   *In-situ* Sr and Nd isotope measurements by fs–LA–MC–ICP–MS were performed on a Neptune

147   Plus MC–ICP–MS (Thermo Fisher Scientific, Germany) in combination with a J-200 343 nm

148   femtosecond (fs) laser ablation system (Applied Spectra, USA) housed at the National Research

149   Center for Geoanalysis, Chinese Academy of Geological Sciences (CAGS), Beijing, China. The

150   instrumental mass bias for Sr isotopes was corrected using an exponential law function based on

---

[1] Deposit item

151   ^{86}Sr/^{88}Sr value of 0.1194. In-house scheelite reference materials HTPW and XJSW (C. Li et al.

152   2018) were analyzed every 10 samples. The in-house scheelite reference material (XWC) and

153   Durango apatite (Foster and Vance 2006; Yang et al. 2014) were analysed for every 10 samples to

154   monitor instrument stability and allow external correction of ^{147}Sm/^{144}Nd ratios. Detailed data

155   processing methodologies are given in Supplemental[1].

RESULTS

Scheelite textures

157

158   Examination of crosscutting and replacement relationships and textural features allowed

159   recognition of five types of scheelite: Sch1 and Sch2 are from Stage 1; Sch3, Sch4, and Sch5 are

160   from Stage 2. Scheelite from Stage 1 displays a complex CL response in that it exhibits areas of

161   primary growth (Sch1) overprinted by a superimposed type (Sch2) (Fig. 5a). Primary Sch1 is

162   relatively dark in CL response, with clear zonation texture. Sch2 commonly overgrows Sch1 and

163   displays a delicate oscillatory zonation pattern defined by multiple individual zones, each varying

164   from several to tens of micrometers in width (Fig. 5a, b).

165   Scheelite from Stage 2 has roughly similar but rather complex textures, including oscillatory,

166   patchy, and evidence of dissolution-reprecipitation reaction (Fig. 5c–f). Sch3 is characterized by a

167   well-developed oscillatory zonation pattern, with fluctuation in zone thickness, ranging from several

168   to tens of micrometers in width (Fig. 5c–f). Some Sch3 grains have a bright zoned core and dark

169   zoned rims on CL images, which is overgrown by homogenous Sch4 (Fig. 5c).

170   Sch4 is commonly homogeneous in CL images (Fig. 5c), although some grains display patchy

171   texture (Fig. 5d, e). Sch4 deposited as rims around Sch3, and the contact boundary between Sch4

172   and Sch3 is either regular (Fig. 5c) or irregular (Fig. 5e); the latter showing overprinting or

173   dissolution-reprecipitation textures.

174   Sch5 shows brighter CL response compared to Sch3 and Sch4, and lacks discernible zonation

175   under CL (Fig. 5c, d). Sch5 either replaces Sch3 (Fig. 5c) or occurs as 'matrix' infilling between

176   Sch3 and Sch4 (Fig. 5d).

177   *Scheelite composition*

178   Trace element concentration data for the five sub-types of scheelite are summarized in Table 1 and

179   presented in Fig. 6; the full dataset is included in Supplemental[1] Table S3.

180   Results show that all five sub-types of scheelite are close to endmember in composition, and that

181   Mo concentrations are mostly below 46 ppm (Fig. 6a). Concentrations of Sr, although overlapping,

182   are variable within any individual type (Fig. 6b, c). Measured Sr concentrations range between 85

183   and 116 ppm for Sch1 (mean 95 ppm), from 49 to 153 ppm for Sch2 (mean 67 ppm), from 42 to

184   193 ppm for Sch3 (mean 73 ppm), from 36 to 118 ppm for Sch4 (mean 71 ppm), and from 42 to

185   1,025 ppm for Sch5 (mean 264 ppm) (Table 1). Sodium concentrations show a narrow range for

186   scheelite from Stage 1 (35~186 ppm), in contrast to the scheelite from Stage 2 that displays a

187   relatively large variation (10 to 300 ppm for Sch3, 9 to 250 ppm for Sch4, and <7 to 174 ppm for

188   Sch5, respectively (Fig. 6d, f).

189   REE concentrations were normalized to chondrite values (McDonough and Sun 1995) and are

190   shown in Figure 7. Analyzed scheelites can be grouped into four distinct types according to their

191   REE patterns: LREE-enriched, MREE-enriched, HREE-enriched, and flat patterns (Fig. 7).

192   Sch1 from Stage 1 (Fig. 5a) features a LREE-enriched pattern with $(La/Yb)_N$ values ranging

193   from 4.6 to 9.6 (Fig. 7a), accompanied by weak positive Eu anomalies (δEu = 1.0 to 2.2). Total

194   REE concentrations range between 938 and 1,172 ppm (mean 1,015 ppm), and the measured Nd

9

195   contents vary between 203 and 248 ppm (mean 220 ppm) (Table 1).

196   Sch2 from Stage 1 is characterized by HREE-enriched pattern with $(La/Yb)_N$ values below 0.4,

197   and both positive and negative Eu anomalies, with Nd concentrations between 41 and 157 ppm

198   (mean 86 ppm) (Table 1). Sch2 overgrowths on Sch1 (Fig. 5a) mostly feature weak positive Eu

199   anomalies (δEu = 0.8 to 1.6) (Fig. 7a, Sample YJS-69), with total REE concentrations between 522

200   and 1,082 ppm (mean 892 ppm) and $(La/Yb)_N$ values ranging from 0.17 to 0.36. In contrast, Sch2

201   occurring as isolated grains (Fig. 5b) has negative Eu anomalies (δEu = 0.2 to 0.9) (Fig. 7a, Sample

202   YJS-87) with total REE concentrations between 524 and 818 ppm (mean 659 ppm), and relatively

203   lower $(La/Yb)_N$ values (0.02 to 0.16).

204   Scheelite from Stage 2 is characterized by site-specific REE fractionation patterns (Fig. 7b–i),

205   with no single distinctive REE pattern recognizable, particularly for the zoned Sch3 sub-type. Sch3

206   features a broad variety of REE patterns (Fig. 7b–f) and both negative and positive Eu anomalies

207   (δEu = 0.2 to 14.7), with $(La/Yb)_N$ values ranging from <0.1 to 10.1. Total REE concentrations

208   range between 184 and 1,801 ppm (mean 911 ppm), and Nd concentrations from 21 to 351 ppm,

209   with a mean value of 154 ppm (Table 1). The distinct micron-scale zones within individual grains

210   (e.g., Sample YJS-55, Fig. 5d) show markedly different REE patterns and variable Eu anomalies

211   (Fig. 7c).

212   Similar to Sch3, Sch4 and Sch5 also display complex REE patterns with $(La/Yb)_N$ values

213   ranging from 0.1 to 8.2, and both positive and negative Eu anomalies (δEu = 0.3 to 20.7 and 0.2 to

214   2.5 for Sch4 and Sch5, respectively) (Fig. 7g–i). Total REE concentrations range from 98 to 1,609

215   ppm for Sch4 (mean 788 ppm), and from 51 to 1,243 ppm for Sch5 (mean 407 ppm). The measured

216   Nd concentrations vary from 10 to 323 ppm for Sch4 (mean 129 ppm), and from 8 to 278 ppm for

217   Sch5 (mean 85 ppm) (Table 1).

10

218 *Trace element mapping*

219 LA–ICP–MS trace-element maps (Figs. 8 and 9) are used to further visualize the chemical

220 heterogeneity behind the observed CL-defined zonation in two representative scheelite grains with

221 complex REE fractionation patterns from Stage 2 (Samples YJS-55 and YJS-67). Scheelite from

222 Stage 1, which has relatively consistent REE fractionation patterns (Fig. 7a), was not mapped.

223   The mapped area from sample YJS-55 contains Sch3, Sch4, and Sch5, and they display

224 contrasting CL intensity (Fig. 8). Sch3 shows distinct chemical heterogeneity for most mapped

225 elements, and is relatively enriched in MREE, HREE, Nb, and Na compared to Sch4 and Sch5.

226 MREE appear to show an oscillatory distribution pattern and show a decoupling between Eu and

227 other elements. Maps for Na, Mn, and Pb show that these elements are enriched as patches rather

228 than across the entire grain. Niobium shows an oscillatory distribution pattern in Sch3, whereas the

229 distribution of Mo is irregular. Compared to Sch3 and Sch5, Sch4 is relatively enriched in La, Ce,

230 Eu, and U. Except for Eu and Lu, other MREE and HREE are at low concentrations. Sch5 is

231 relatively depleted in all trace elements except Sr. Interestingly, the distribution of Sr does not

232 follow the same chemical zones as delineated by other elements (e.g., REE, Mo, and Mn).

233   Sample YJS-67 contains Sch3 with a pronounced oscillatory zoning (Fig. 9). The upper part of

234 the mapped area appears brighter than the lower part in CL image. This difference in brightness

235 may, however, be an artefact arising from the electron-beam detector geometry. Although the two

236 parts of the grain appear discontinuous in the CL image, element maps show a continuous

237 distribution of most elements, including MREE, HREE, Mo, Nb and U, across the boundary

238 between the two domains. The maps reveal a large variability in REE concentrations between zones,

239 and, moreover, a discontinuous distribution of LREE (La, Ce, and Pr) within zones. We also note

240 that Eu is relatively enriched in the inner zones, in contrast to the distribution patterns shown by Mo

11

241 and Pb. Mapping also reveals that Na, Mn, and Sr are irregularly distributed.

242 *In-situ Sr-Nd isotope composition of scheelite*

243 Sr-Nd isotope data for scheelites from the Yangjiashan deposit are summarized in Tables 2 and 3,

244 respectively, and shown as Figure 10. The full dataset is included as Supplemental[1] Tables S4 and

245 S5. All Nd isotope compositions were also recalculated to 400 Ma (Xie et al. 2019a) due to decay of

246 ^{147}Sm to generate ^{143}Nd. Measured values for Durango apatite and other reference materials match

247 standard values well. Together with the good reproducibility, any possibility of analytical artefacts

248 can be precluded. Depending on Sr content, the signal intensity for ^{88}Sr ranges from 0.31 to 5.81 V

249 (Fig. 10a), The uncertainty of all ^{87}Sr/^{86}Sr values varied from 0.00007 to 0.0009 (2σ), displaying an

250 inverse correlation with Sr content, which is manifested by the signal intensity of ^{88}Sr (Fig. 10a).

251 Initial ^{87}Sr/^{86}Sr ratios for Sch1 to Sch5 range from 0.71336 to 0.72617 (Fig. 10b). The

252 ^{147}Sm/^{144}Nd and ^{143}Nd/^{144}Nd ratios for Sch1 to Sch5 are from 0.09147 to 0.29343, and from

253 0.51085 to 0.51173, respectively (Fig. 10c). Calculated initial εNd(t) values range from -24.9 to -7.7

254 (Fig. 10d).

255 **DISCUSSION**

256 *Correlation between textures observable by CL imaging and trace element distributions*

257 Combining trace element maps with textures imaged by CL gives invaluable insights into the nature

258 of ore-forming fluids and allows reconstruction of the growth history of minerals like scheelite.

259 Scales of observation and spatial resolutions are similar, allowing direct comparison between

260 element concentrations and CL intensity over relatively large areas of individual grains.

261 The role played by Mo in modifying the intensity of the CL response of scheelite remains

262 uncertain. In samples studied here, Mo-depleted Sch5 domains have a brighter CL response than

12

263   Mo-enriched Sch3 and Sch4 (Fig. 8), consistent with the observation that a decrease in the CL

264   intensity occurs with increased Mo content due to a greater distortion of the crystal structure (Poulin

265   et al. 2016). We speculate, however, that while this correlation is essentially correct, it may not be

266   exclusively so because some fluctuations of CL intensity occur independently of Mo concentration

267   variation when Mo concentrations in scheelite reach >10,000 ppm, such as in the Zinnwald–

268   Cínovec Sn–W–Li greisen-type deposit, Germany-Czech Republic (Poulin et al. 2016). LA–ICP–

269   MS element maps of scheelite from the Dabaoshan porphyry Mo–W deposit, South China (Su et al.

270   2019), also reveal more complex relationships between CL intensity and Mo content. We therefore

271   conclude that substitution of Mo for W, at the grain-scale, has an inconsistent effect on the CL

272   response of scheelite. Although incorporation of Mo will decrease the self-activated emission band

273   effectiveness that is correlated to W content, other factors such as incorporation of REE and Pb

274   which cause lattice distortion, all have influence on CL response (Macrae and Wilson 2009; Poulin

275   et al. 2016).

276   Whether Sr plays a role in modifying the intensity of the CL response of scheelite remains

277   unclear thus far, even though data compilations have shown that scheelite from different geological

278   settings can be distinguished by markedly different Sr content and REE characteristics (Poulin et al.

279   2018; Sciuba et al. 2020). For example, a maximum of 11,480 ppm, and mean value of ~2,232 ppm

280   Sr has been given for orogenic gold deposits compared to an overall average of 387 ppm for

281   magmatic-hydrothermal deposits (Poulin et al. 2018). The maps of Sch3 with oscillatory variation

282   in CL intensity among growth zones (Figs. 8 and 9) show no concordant measurable variation in Sr

283   concentration. Both positive or negative correlation between Sr concentration and CL intensity have

284   been observed elsewhere (Poulin et al. 2016; Su et al. 2019). Collectively, these observations

285   suggest no direct cause and effect relationship between Sr concentration and CL intensity within

13

286   individual scheelite grains, although incorporation of Sr might cause intrinsic defects in scheelite

287   due to its electronic configuration (Poulin et al. 2016).

288   Incorporation of REE has also been demonstrated to exert an influence on CL intensity, and

289   scheelite from different mineralization settings can be distinguished by their CL textures and REE

290   fractionation patterns. For example, scheelite from orogenic gold deposits commonly shows

291   homogenous CL images and has a MREE-enriched but otherwise flat pattern (Poulin et al. 2016;

292   Sciuba et al. 2020). Likewise, LREE-enriched patterns appear to be a feature of

293   magmatic-hydrothermal deposits such as skarns and porphyry systems. Scheelite from these

294   deposits are characterized by complex (e.g., oscillatory) CL responses (Song et al. 2014, 2019;

295   Poulin et al. 2016; Sun and Chen 2017; Zhao et al. 2018). Figures 8 and 9 show no general

296   relationship between scheelite CL intensity and REE concentrations, highlighting the interplay

297   between individual REE^{3+}, such as Eu and Tb. In other words, the resulting CL response depends on

298   the intensity ratios of these activators and is thus not an unambiguous characteristic of one element

299   or the other (Nazarov et al. 2004; Macrae et al. 2009; Götze 2012). Our study nevertheless provides

300   'snapshot' information about the importance of element maps in revealing the heterogeneous

301   distribution of REE in scheelite displaying complex CL intensity variation. Because our analyses

302   reflect bulk CL intensities (the combined result of CL intensities at different spectral emissions),

303   and due to a lack of qualitative CL spectra data, an unequivocal determination of which REE plays

304   the most important role in controlling the CL response observed is hindered.

305   In summary, except for the overwhelming nature of the self-luminescence band attributed to

306   WO_4^{2-} tetrahedra, trace elements incorporated into scheelite, including Mo, Sr, or REE, have, by

307   themselves only inconsistent effects on the CL response. Both intrinsic (e.g., the self-activated

308   emission band and structural defects) and extrinsic defects (e.g., trace element incorporation) are

14

309   responsible for the CL response (Macrae et al. 2009; Götze 2012; Poulin et al. 2016).

310   *Origin of distinct REE fractionation patterns*

311   The various measured REE fractionation patterns in scheelite from the Yangjiashan deposit suggests

312   that although there are clearly generalized trends with global significance as summarized above,

313   heterogeneity within a single deposit, or even among grains in the same sample, may show variation

314   that overlaps with these general trends (Fig. 7). We suggest that coexisting Ca-bearing minerals and

315   temperature both have insignificant effects on REE fractionation.

316   Previous studies have shown that the presence of coexisting Ca-bearing minerals such as garnet

317   and diopside can impact on the REE fractionation patterns of scheelite, particularly in skarns (e.g.,

318   Song et al. 2014; Zhao et al. 2018). We examined the mineral assemblages associated with scheelite

319   and note that the most abundant minerals associated with scheelite are quartz and sulfides

320   (arsenopyrite and pyrite) (Fig. 4), accompanied by very small amounts of fluorite (Fig. 4c).

321   Consequently, we anticipate no significant change in the concentrations of REE in fluid and

322   negligible impact on the preferred partitioning of LREE or HREE to be induced by the presence of

323   Ca-bearing minerals. Temperature is an important control on the mobility of the REE in fluid

324   (Migdisov et al. 2016). We discount the temperature factor because measured homogenization

325   temperatures are mostly within a narrow range (200 to 270 °C; Xie et al. 2019a).

326   We propose that: (1) fluid compositions; (2) different substitution mechanisms; and (3)

327   hydrothermal replacement processes (e.g., dissolution-reprecipitation) are all responsible for the

328   range of REE fractionation patterns observed in Yangjiashan scheelite. The development of

329   wall-rock alteration accompanying vein formation, combined with the extreme variations in Sr and

330   Nd isotope compositions in the Yangjiashan deposit (Fig. 10), provide evidence for an open

331   mineralizing system. Published case studies have shown that, in a closed system, scheelite shows

332   gradual changes from MREE-enriched to MREE-depleted patterns (Brugger et al. 2000). Changes

333   in REE fractionation patterns in this study cannot be explained by the closed system crystallization

334   advocated by Brugger et al. (2000).

335   (1) **Fluid composition**. Sch1 and the Baimashan pluton have similar REE patterns (Fig. 7a),

336   suggesting that scheelite inherits its REE composition from the ore-forming fluid, a plausible

337   explanation that has been applied in the interpretation of some W skarns (e.g., Song et al. 2014; Sun

338   and Chen 2017). In addition, scheelite preferentially incorporates LREE over HREE due to ionic

339   radii considerations (Poulin et al. 2018), a potential mechanism that contributes to the observed

340   LREE-enrichment in Sch1. Calculated LREE/HREE values for granite and Sch1 range from 4.2 to

341   16.9 (with a mean value of 12.3; Yang et al. 2015), and from 5.9 to 10.1 (with a mean value of 8.1;

342   Supplemental[1] Table S3), respectively. Sch1 crystallization, assuming low fluid-rock interaction

343   during Stage 1, would shift the residual fluid to relative LREE enrichment, thus allowing deposition

344   of HREE-depleted Sch2. However, this is in contrast with HREE-enriched Sch2 (Fig. 7a),

345   indicating that the original magmatic REE signature has been modified during fluid-rock interaction,

346   a process that is supported by the Sr and Nd isotope signatures (Fig. 10b, d).

347   (2) **Different charge balance mechanisms**. The substitution $REE^{3+} \leftrightarrow Ca^{2+}$ is not isovalent,

348   hence, a mechanism of charge balance is required. Three main mechanisms for REE substitution of

349   Ca have been proposed (Nassau and Loiacono 1963; Ghaderi et al. 1999; Brugger et al. 2000):

$$Ca^{2+} + W^{6+} = REE^{3+} + Nb^{5+} \ (1);$$

$$2Ca^{2+} = REE^{3+} + Na^{+} \ (2);$$

$$3Ca^{2+} = 2REE^{3+} + \square Ca, \text{ where } \square Ca \text{ is a Ca-site vacancy (3)}.$$
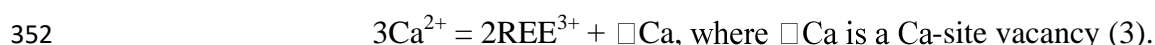
353   For mechanism (1), binary plots of the mole fraction of REE against Nb display a generally

354 positive correlation, and some spots of Sch2, Sch3 and Sch5 are close to the 1:1 correlation line

355 (Fig. 6e). This indicates that the coupled substitution in equation (1) are applicable to some

356 scheelites (Zhao et al. 2018). This hypothesis is further supported by relatively high concentrations

357 of Nb, exceeding 240 ppm (Fig. 6e). Given the fact that the radius of Nb^{5+} (0.48 Å) is closer to that

358 of Mo^{5+} (0.46 Å) than Mo^{6+} (0.41 Å) (Shannon 1976), incorporation of Nb could have been coupled

359 to the concentration of Mo^{5+} in scheelite under relatively reduced conditions (Zhao et al. 2018). We

360 also note that Nb incorporation may favor substitution of HREE or MREE over LREE based on

361 spot and mapping results (Figs. 8 and 9), leading to a series of diverse REE patterns (Fig. 6e).

362 For mechanism (2), Ghaderi et al. (1999) and Brugger et al. (2000) suggested that if Na in the

363 fluid is sufficiently high (>60 ppm) to provide the charge balance in scheelite, considering that Na

364 can incorporated into scheelite based on Goldschmidt's rules (Na^{1+} = 1.18Å, Ca^{2+} = 1.12 Å;

365 Shannon 1976), MREE would preferentially substitute into the Ca site. In this study, some Sch1 and

366 Sch5 plot close to the ideal 1:1 correlation line (Fig. 6f), supporting the coupled substitution in

367 equation (2). Most data plot away from the 1:1 correlation line, however (Fig. 6f), indicating that

368 equation (2) cannot be the dominant substitution mechanism.

369 For mechanism (3), we prefer to explain the flat REE patterns (Fig. 7e) in terms of REE

370 incorporation in scheelite via a Ca-site vacancy mechanism, enabling REE^{3+} incorporation into

371 these scheelites independently of ionic radius (Nassau and Loiacono 1963; Ghaderi et al. 1999).

372 Changes from MREE-enriched patterns to flat patterns via the fractional crystallization model

373 proposed by Brugger et al. (2000) might be unsuitable for the Yangjiashan deposit, because

374 significant changes in pattern are observed from scheelite with oscillatory texture (Fig. 11). Shifting

375 a local maximum from MREE to HREE is more likely to be related to site distortion in the Ca^{2+} site

376 caused by the replacement of Ca^{2+} by Sr^{2+} or other elements with relatively large ionic radii such as

17

377   the detectable Pb^{2+} (Ghaderi et al. 1999; Poulin et al. 2018).

378   (3) **Primary-secondary processes.** Scheelite with primary textures such as oscillatory zoning

379   and secondary textures such as evidence for dissolution-reprecipitation reaction (Figs. 5 and 11),

380   provide an opportunity to illustrate REE behavior during these processes. It has been suggested that

381   oscillatory zoning is either caused by extrinsic changes in the parent hydrothermal system, such as

382   varying fluid composition, pressure or temperature, or is associated with intrinsic mechanisms

383   linked to diffusion and growth rate (Loomis 1983; Shore and Fowler 1996). Scheelite with

384   oscillatory texture showing either insignificant or significant variations in REE patterns among

385   different grains (Fig. 11a–d), may suggest that the REE signatures alone cannot be used to make

386   inferences about extrinsic chemical changes in the fluid from which scheelite precipitated. If REE

387   enters these scheelite grains via coupled extrinsic and intrinsic mechanisms, the validation of which

388   warrants further investigation, it becomes more difficult to clearly link information recorded by the

389   REE to ore-forming processes. The data for scheelite from the Yangjiashan deposit represents an

390   example of how the REE patterns of Ca-minerals with complex grain-scale textures (e.g., apatite)

391   can be linked to hydrothermal processes and identify the fluid source. The complex patterns do,

392   however, challenge the role of REE fractionation patterns as a discriminator of ore deposit genesis.

393   Moreover, the observed dissolution-reprecipitation textures hint at REE mobility during

394   secondary processes. Sch5 occurring within Sch3 that may have formed via

395   dissolution-reprecipitation processes shares similar REE fractionation patterns to those of the

396   precursor Sch3 (Fig. 11e, f). In contrast to these, Sch5 precipitated as overprinting rims has a

397   distinct REE fractionation patterns compared to earlier types (Fig. 11g, h). Such a contrast in REE

398   fractionation patterns for these two types of Sch5 reflect the multiple controlling factors on REE

399   properties as discussed above.

18

400   *Source and nature of ore-forming metals and fluids*

401   Age-corrected (400 Ma) initial whole rock $^{87}Sr/^{86}Sr$ ratios and εNd(t) isotope composition of the

402   Banxi Group slate display wide ranges (0.71085 to 0.73462 and -16.6 to +0.3, respectively),

403   overlapping that of the Baimashan intrusion (0.71671 to 0.71682 and -12.2 to -12.0, respectively;

404   Supplemental[1] Tables S6 and S7) (Fig. 10b, d). The Baimashan granite has been interpreted to be

405   derived from partial melting of Neoproterozoic crustal rock (Shu et al. 2006; Chu et al. 2012).

406   Several lines of evidence support a close genetic relationship between mineralization and the host

407   granite. These include: (1) overlapping ages − intrusion and mineralization both took place at ~404

408   Ma (Xie et al. 2019a); (2) isotope compositions, such as the H and O isotope signatures of quartz,

409   indicating that ore-forming fluids originated mainly from granite, with input of meteoric water (Xie

410   et al. 2019a); and (3) similar REE pattern of Sch1 and the Yangjiashan granite (Fig. 7a). We deduce

411   that the most probable source of Sr and Nd for all scheelite sub-types is a mixing of

412   magmatic-hydrothermal fluids following interaction with host rock (Fig. 10b, d).

413   The accurate determinations of *in-situ* Sr-Nd isotope compositions by fs–LA–MC–ICP–MS (C.

414   Li et al. 2018), make it an ideal method for tracing the fluid evolution path and for estimation of the

415   source of ore-forming metals (Foster and Vance 2006; Yang et al. 2011, 2014; Kozilk et al. 2016). In

416   the Yangjiashan deposit, the different populations of $^{87}Sr/^{86}Sr$ ratios in scheelite show a broadly

417   decreasing trend from Sch2 to Sch5 (Fig. 10b). The broadly decreasing Sr isotope compositions

418   may be explained as follows. (1) Scheelite from greisen ores (Stage 1) was precipitated under a

419   more intensive wall rock alteration regime than scheelite from quartz veins (Stage 2). The structural

420   control of quartz veins indicates channelized fluid migration along faults or cracks (Sibson 1994;

421   Robb 2005). A greater proportion of Sr from wallrock is recorded in Stage 1 than Stage 2. (2) The

422   Neoproterozoic Banxi Group slate displays a very large range of Sr isotope compositions (Fig. 10b),

423   therefore, incongruent leaching of radiogenic Sr in altered host rock may have contributed to this

424   (Mueller et al. 1991; Darbyshire et al. 1996; Kempe et al. 2001; Glodny and Grauert 2009). Similar

425   conclusions have been reached to interpret the regional Sr isotope variations in scheelite from

426   orogenic Au–W deposits hosted in greenschist/grayschist with different Sr isotope composition,

427   Otago Schist, New Zealand (Scanlan et al. 2018).

428   The εNd(t) data for Sch1 and a sub-population of Sch2 are depleted relative to the Baimashan

429   granite, indicating mixing with Banxi Group slate with low εNd(t) values during Stage 1 (Fig. 10d).

430   The εNd(t) values for Sch3 range widely, and together with the oscillatory textures in these

431   scheelite types, point to a primary origin for the isotopic variations, i.e., they reflect isotopic

432   variations in the hydrothermal fluids from which the scheelite precipitated (Brugger et al. 2002).

433   The large variation of εNd(t) values, particularly for these low εNd(t) values, are distinct from the

434   age-corrected (400 Ma) εNd(t) values of the Banxi Group slate (Fig. 10d). Fluorite (Fig. 4c) and

435   REE-bearing minerals occur as inclusions within scheelite (Supplemental[1] Fig. A1). Both are

436   candidates that could induce similar effects as bastnäsite (Brugger et al. 2002), in that their

437   deposition would disturb the Sm/Nd ratio of ore-forming fluid, causing an erroneous extrapolation

438   from measured ^{143}Nd/^{144}Nd to a spurious initial ^{143}Nd/^{144}Nd at 400 Ma. Similar cases have been

439   observed in scheelite from gold deposits, for example, anomalous εNd(t) signatures described by

440   Ghaderi (1998) and Brugger et al. (2002). The two endmember modeling results indicate that the

441   measured Sr and Nd isotope compositions of scheelite show deviation from the mixing line (Fig.

442   12), providing an additional indication that disturbance of the Sm/Nd ratio in fluid contributed to

443   the large variation observed.

444   At Stage 1, although the REE pattern of the Yangjiashan granite and Sch1 are similar, their δEu

445   values are distinct: negative for granite (0.52~0.71; Yang et al. 2015); and neutral or positive for

20

446   Sch1 (1.0~2.2; Fig. 6a). This difference in the sign of Eu anomalies may reflect hydrothermal fluids

447   with some modifications by reaction with wall rock and input of meteoric water (Brugger et al.

448   2002; Sun and Chen 2017). This is supported by the fact that the greisen mineralization is the

449   product of fluid interaction with wall rock (Fig. 4a, b) and the H and O isotope signatures (Xie et al.

450   2019a).

451   During Stage 2, we propose that local pH fluctuation is responsible for the complex Eu

452   anomalies observed. Case studies have shown that the oxidation state of trace elements (e.g., Eu)

453   incorporated in hydrothermal minerals provides an additional tool to constrain the nature of fluids,

454   such as pH (Brugger et al. 2008). According to modelling (Brugger et al. 2008), results show that

455   under the same fO_2 and temperature, a drop/increase in fluid pH of ~0.3 unit will lead to the

456   Eu^{2+}/Eu^{3+} ratios in scheelite shifting from 1.0 to 7.3, hence, the oxidation state of Eu in scheelite

457   could be a sensitive tracer of fluid pH. During fluid-rock interaction, mixing with meteoric water,

458   together with fluid boiling processes resulting in loss of CO_2 (Supplemental[1] Fig. A2), fluid pH will

459   change (Wood and Samson 2000), causing large variations in the size of Eu anomalies in scheelite

460   (Fig. 13). Progressive fluid-rock interaction is also manifested by the *in-situ* Sr and Nd isotope

461   signatures discussed above. The lower total REE concentrations of Sch5 (Fig. 11g, h) may also

462   record mixing with meteoric water, a component that normally has very low REE contents. Input of

463   meteoric water is further evidenced by the H-O isotope compositions of quartz coexisting with

464   scheelite (Xie et al. 2019a). Changes in fluid redox state related to the variations in the Eu^{2+}/Eu^{3+}

465   ratios preserved in scheelite is negligible, considering scheelite in the Yangjiashan deposit

466   precipitated from relatively reduced fluids with narrow ranges in fO_2 (Supplemental[1] Fig. A3).

Implications for the study of scheelite

Firstly, coupled *in-situ* Sr-Nd isotope analyses are of great advantage in illustrating the source of ore-forming metals and tracing dynamic hydrothermal processes. In this study, the Sr-Nd isotope compositions for all types of scheelite display relatively large variations, particularly for Sch3, which displays oscillatory texture and complex REE fractionation patterns (Fig. 11). These variations implicitly suggest that conventional bulk powder analysis of Sr and Nd isotope compositions may be problematic for texturally complicated scheelite.

Secondly, Sm-Nd dating of scheelite should be carried out with caution. Absolute age determinations using the Sm-Nd isotope system assume that the fluid is homogeneous with respect to initial $^{143}Nd/^{144}Nd$, and that minerals have remained closed systems with respect to Sm and Nd since crystallization (Dickin 2005). This study suggests that a fluid system with heterogeneous $^{143}Nd/^{144}Nd$ and $^{147}Sm/^{144}Nd$ composition for texturally complex scheelite also challenges the meaning of Sm-Nd scheelite ages (Fig. 10c). For example, in the Mount Charlotte Au ± W deposit, the Sm-Nd scheelite age of 2,772 ± 86 Ma determined by conventional bulk powder methods (Kent et al. 1995), is older than the age of hydrothermal muscovite (2,602 ± 8 Ma; Kent and McDougall 1995). These different ages and the corresponding time gaps between metamorphism, magmatism and Au mineralization contribute to the observed diversity of ages and equivocality on ore genesis. We suggest that micron- to nano-scale textural investigation, together with a preliminary round of (fs)-LA–ICP–MS trace element analysis to determine variations in Sm and Nd concentrations and isotope ratios, should be undertaken prior to conducting conventional or *in-situ* Sm-Nd isotope analysis. Grains or points should be selected for isotopic analysis to cover the full range of Sm/Nd ratios present.

CONCLUSIONS

489

490   1. Fluid compositions, different substitution mechanisms, primary, and secondary processes, all

491   contribute to the variation in observed REE fractionation patterns. Concentrations of Mo, Sr, or

492   REE in scheelite cannot individually be linked to differences in CL intensity. Local pH fluctuation

493   is suggested to be responsible for complex Eu anomalies.

494   2. Large variations in Sr and Nd isotope compositions of scheelite suggest that the Yangjiashan

495   deposit derived from a mixing of magmatic-hydrothermal fluids following interaction with the

496   Neoproterozoic slate. Fluid-rock interaction, changes in fluid composition, and a disturbance of

497   Sm/Nd ratios in fluid induced by precipitation of fluorite and REE-bearing minerals. Each of these

498   factors contribute to the observed large variations in Sr and Nd isotope compositions. Sm-Nd dating

499   of scheelite should be carried out with caution and an in-depth understanding of the grains selected

500   for analysis.

501   3. Texturally-complex scheelite provides critical information on the dynamics of hydrothermal

502   systems, highlighting the value of combining LA–ICP–MS mapping and *in-situ* Sr-Nd isotopes

503   analysis on well characterized samples to illustrate the source of ore-forming metals and trace

504   evolving hydrothermal processes.

REFERENCES

515   Barker, S.L.L., and Cox, S.F. (2011) Oscillatory zoning and trace element incorporation in hydrothermal

516   minerals: Insights from calcite growth experiments. Geofluids, 11, 48–56.

517   Bell, K., Anglin, C.D., and Franklin, J.M. (1989) Sm-Nd and Rb-Sr isotope systematics of scheelites:

518   Possible implications for the age and genesis of vein-hosted gold deposits. Geology, 17, 500–504.

519   Brugger, J., Etschmann, B., Pownceby, M., Liu, W.H., Grundler, P., and Brewe, D. (2008) Oxidation state of

520   europium in scheelite: Tracking fluid-rock interaction in gold deposits. Chemical Geology, 257, 26–33.

521   Brugger, J., Lahaye, Y., Costa, S., Lambert, D., and Bateman, R. (2000) Inhomogeneous distribution of REE

522   in scheelite and dynamics of Archaean hydrothermal systems (Mt. Charlotte and Drysdale gold deposits,

523   western Australia). Contributions to Mineralogy and Petrology, 139, 251–264.

524   Brugger, J., Mass, R., Lahaye, Y., Mcrae, C., Ghaderi, M., Costa, S., Lambert, D., Bateman, R., and Prince,

525   K. (2002) Origins of Nd-Sr-Pb isotopic variations in single scheelite grains from Archaean gold

526   deposits, western Australia. Chemical Geology, 182, 203–225.

527   Chu, Y., Lin, W., Faure, M., Wang, Q., and Ji, W. (2012) Phanerozoic tectonothermal events of the

528   Xuefengshan belt, central south China: Implications from U-Pb age and Lu-Hf determinations of

529   granites. Lithos, 150, 243–255.

530   Ciobanu, C.L., Cook, N.J., Maunders, C., Wade, B.P., and Ehrig, K. (2016) Focused ion beam and advanced

531   electron microscopy for minerals: Insights and outlook from bismuth sulphosalts. Minerals, 6, 112;

532   doi:10.3390/min6040112.

533   Cook, N.J., Ciobanu, C.L., Ehrig, K., Slattery, A., Verdugo-Ihl, M.R., Courtney-Davies, L., and Gao, W.Y.

534   (2017) Advances and opportunities in ore mineralogy. Minerals, 7, 233; doi:10.3390/min7120233.

535   Cook, N.J., Ciobanu, C.L., and Mao, J. (2009) Textural control on gold distribution in As-free pyrite from

536   the Dongping, Huangtuliang and Hougou gold deposits, north China craton (Hebei province, China).

537   Chemical Geology, 264, 101–121.

538   Cook, N.J., Ciobanu, C.L., Meria, D., Silcock, D., and Wade, B.P. (2013) Arsenopyrite-pyrite association in

539 an orogenic gold ore: Tracing mineralization history from textures and trace elements. Economic

540 Geology, 108, 1273–1283.

541 Darbyshire, D.P.F., Pitfield, P.E.J., and Campbell, S.D.G. (1996) Late Archean and Early Proterozoic

542 gold-tungsten mineralization in the Zimbabwe Archean craton: Rb-Sr and Sm-Nd isotope constraints.

543 Geology, 24, 19–22.

544 Dickin, A.P. (2005) Radiogenic isotope geology, 2nd edition, 509 p. Cambridge University Press, U.K.

545 Foster, G.L., and Vance, D. (2006) In situ Nd isotopic analysis of geological materials by laser ablation

546 MC-ICP-MS. Journal of Analytical Atomic Spectrometry, 21, 288–296.

547 Fougerouse, D., Micklethwaite, S., Tomkins, A.G., Mei, Y., Kilburn, M., Guagliardo, P., Fisher, L.A.,

548 Halfpenny, A., Gee, M., Paterson, D., and Howard, D.L. (2016) Gold remobilisation and formation of

549 high grade ore shoots driven by dissolution-reprecipitation replacement and Ni substitution into

550 auriferous arsenopyrite. Geochimica et Cosmochimica Acta, 178, 143–159.

551 Ghaderi, M. (1998) Source of Archaean gold mineralization in the Kalgoorlie-Norseman region of western

552 Australia, determined from strontium-neodymium isotopes and trace elements in scheelite and host

553 rocks. Ph.D. thesis, The Australian National University, Australia.

554 Ghaderi, M., Palin, J.M., Campbell, I.H., and Sylvester, P.J. (1999) Rare earth element systematics in

555 scheelite from hydrothermal gold deposits in the Kalgoorlie-Norseman region, western Australia.

556 Economic Geology, 94, 423–437.

557 Glodny, J., and Grauert, B. (2009) Evolution of a hydrothermal fluid-rock interaction system as recorded by

558 Sr isotopes: A case study from the Schwarzwald, SW Germany. Mineralogy and Petrology, 95, 163–

559 178.

560 Götze, J. (2012). Application of cathodoluminescence microscopy and spectroscopy in geosciences.

561 Microscopy and Microanalysis, 18, 1270–1284.

562 Hu, R.Z., Fu, S.L., Huang, Y., Zhou, M.F., Fu, S.H., Zhao, C.H., Wang, Y.J., Bi, X.W., and Xiao, J.F. (2017)

563 The giant south China Mesozoic low-temperature metallogenic domain: Reviews and a new

564 geodynamic model. Journal of Asian Earth Sciences, 137, 9–34.

565 Kempe, U., Belyatsky, B.V., Krymsky, R.S., Kremenetsky, A.A., and Ivanov, P.A. (2001) Sm-Nd and Sr

566 isotope systematics of scheelite from the giant Au(-W) deposit Muruntau (Uzbekistan): Implications for

567 the age and sources of Au mineralization. Mineralium Deposita, 36, 379–392.

568 Kent, A.J.R., Campbell, I.H., and McCulloch, M.T. (1995) Sm-Nd systematics of hydrothermal scheelite

569   from the mount charlotte mine, Kalgoorlie, western Australia: An isotopic link between gold

570   mineralization and komatiites. Economic Geology, 90, 2329–2335.

571 Kent, A.J.R., and McDougall, I. (1995) ^{40}Ar-^{39}Ar and U-Pb age constrains on the timing of gold

572   mineralization in the Kalgoorlie gold field, western Australia. Economic Geology, 90, 845–859.

573 Kozlik, M., Gerdes, A., and Raith, J.G. (2016) Strontium isotope systematics of scheelite and apatite from

574   the Felbertal tungsten deposit, Austria–results of in-situ LA–MC–ICP–MS analysis. Mineralogy and

575   Petrology, 110, 11–27.

576 Lecumberri-Sanchez, P., Vieira, R., Heinrich, C.A., Pinto, F., and Wälle, M. (2017) Fluid-rock interaction is

577   decisive for the formation of tungsten deposits. Geology, 45, 579–582.

578 Li, C., Zhou, L.M., Zhao, Z., Zhang, Z.Y., Zhao, H., Li, X.W., and Qu, W.J. (2018) In-situ Sr isotopic

579   measurement of scheelite using fs–LA–MC–ICPMS. Journal of Asian Earth Sciences, 160, 38–47.

580 Li, W., Cook, N.J., Xie, G.Q., Mao, J.W., Ciobanu, C.L., Li, J.W., and Zhang, Z.Y. (2019) Textures and

581   trace element signatures of pyrite and arsenopyrite from the Gutaishan Au–Sb deposit, south China.

582   Mineralium Deposita, 54, 591–610.

583 Li, W., Xie, G.Q., Mao, J.W., Zhang, Z.Y., Fu, B., and Lu, S. (2018) Muscovite ^{40}Ar/^{39}Ar and in situ sulfur

584   isotope analyses of the slate-hosted Gutaishan Au–Sb deposit, south China: Implications for possible

585   Late Triassic magmatic-hydrothermal mineralization. Ore Geology Reviews, 101, 839–853.

586 Loomis, T.P. (1983) Compositional zoning of crystals: A record of growth and reaction history. In S. K.

587   Saxena, Ed., Kinetics and Equilibrium in Mineral Reactions. p. 1–60. Springer-Verlag, New York.

588 Macrae, C.M., Wilson, N.C., and Brugger, J. (2009) Quantitative cathodoluminescence mapping with

589   application to a Kalgoorlie scheelite. Microscopy and Microanalysis, 15, 222–230.

590 McDonough, W.F., and Sun, S.S. (1995) The composition of the Earth. Chemical Geology, 120, 223–253.

591 Migdisov, A., Williams-Jones, A.E., Brugger, J., and Caporuscio, F.A. (2016) Hydrothermal transport,

592   deposition, and fractionation of the REE: Experimental data and thermodynamic calculations. Chemical

593   Geology, 439, 13–42.

594 Mueller, A.G., De Laeter, J.R., and Groves, D.I. (1991) Strontium isotope systematics of hydrothermal

595   minerals from epigenetic Archean gold deposits in the Yilgarn block, western Australia. Economic

596   Geology, 86, 780–809.

597 Nassau, K., and Loiacono, G.M. (1963) Calcium tungstate-III: Trivalent rare earths substitution. Journal of

598   Physics and Chemistry of Solids, 24, 1503–1510.

599   Nazarov, M.V., Jeon, D.Y., Kang, J.H., Popovici, E.J., Muresan, L.E., Zamoryanskaya, M.V., and Tsukerblat,

600   B.S. (2004) Luminescence properties of europium-terbium double activated calcium tungstate phosphor.

601   Solid State Communications, 131, 307–311.

602   Poulin, R.S., Kontak, D.J., McDonald, A., and McClenaghan, M.B. (2018) Assessing scheelite as an

603   ore-deposit discriminator using its trace-element and REE chemistry. The Canadian Mineralogist, 56,

604   265–302.

605   Poulin, R.S., McDonald, A.M., Kontak, D.J., and McClenaghan, M.B. (2016) On the relationship between

606   cathodoluminescence and the chemical compositions of scheelite from geologically diverse ore-deposit

607   environments. The Canadian Mineralogist, 54, 1147–1173.

608   Robb, L. (2005) Introduction to Ore-forming Processes, 416 p. Blackwell Publishing, U.K.

609   Rusk, B., and Reed, M. (2002) Scanning electron microscope–cathodoluminescence analysis of quartz

610   reveals complex growth histories in veins from the Butte porphyry copper deposit, Montana. Geology,

611   30, 727–730.

612   Scanlan, E.J., Scott, J.M., Wilson, V.J., Stirling, C.H., Reid, M.R., and Le Roux, P.J. (2018) In situ $^{87}Sr/^{86}Sr$

613   of scheelite and calcite reveals proximal and distal fluid-rock interaction during orogenic W–Au

614   mineralization, Otago Schist, New Zealand. Economic Geology, 113, 1571–1586.

615   Sciuba, M., Beaudoin, G., Grzela, D., and Makvandi, S. (2020) Trace element composition of scheelite in

616   orogenic gold deposits. Mineralium Deposita, 55, 1149–1172.

617   Shannon, R.D. (1976) Revised effective ionic radii and systematic studies of interatomie distances in halides

618   and chalcogenides. Acta Crystallographica, A32, 751–767.

619   Shore, M., and Fowler, A.D. (1996) Oscillatory zoning in minerals: A common phenomenon. The Canadian

620   Mineralogist, 34, 1111–1126.

621   Shu, L.S. (2006). Predevonian tectonic evolution of south China: From Cathaysian block to Caledonian

622   period folded orogenic belt. Geological Journal of China Universities, 12, 418–431 (in Chinese with

623   English abstract).

624   Sibson, R.H. (1994) Crustal stress, faulting and fluid flow. In J. Parnell (ed.), Geofluids: Origin, Migration

625   and Evolution of Fluids in Sedimentary Basins. Geological Society, Special Publication, 78, 69–84.

626   Song, G.X., Qin, K.Z., Li, G.G., Evans, N.J., and Chen, L. (2014) Scheelite elemental and isotopic signatures:

627   Implications for the genesis of skarn-type W–Mo deposits in the Chizhou area, Anhui province, eastern

628   China. American Mineralogist, 99, 303–317.

629 Song, G.X., Cook, N.J., Li, G.M., Qin, K.Z., Ciobanu, C.L., Yang, Y.H., and Xu, Y.X. (2019) Scheelite
630   geochemistry in porphyry-skarn W–Mo systems: A case study from the Gaojiabang deposit, east China.
631   Ore Geology Reviews, 113; doi.org/10.1016/j.oregeorev.2019.103084.

632 Su, K.M., LV, S.J., Kong, L.P., Yang, F.Q., and Xiang, J.F. (2016) Geological characteristics, metallogenetic
633   regularity and model of quartz vein type tungsten deposits in Chongyangping, Hunan province. Mineral
634   Deposits, 35, 902–912 (in Chinese with English abstract).

635 Su, S.Q., Qin, K.Z., Li, G.M., Olin, P., and Thompson, J. (2019) Cathodoluminescence and trace elements of
636   scheelite: Constraints on ore forming processes of the Dabaoshan porphyry Mo–W deposit, south China.
637   Ore Geology Reviews, 115; doi.org/10.1016/j.oregeorev.2019.103183.

638 Sun, K.K., and Chen, B. (2017) Trace elements and Sr-Nd isotopes of scheelite: Implications for the W–Cu–
639   Mo polymetallic mineralization of the Shimensi deposit, south China. American Mineralogist, 102,
640   1114–1128.

641 Wood, S.A., and Samson, I.M. (2000) The hydrothermal geochemistry of tungsten in granitoid environments:
642   I. relative solubilities of ferberite and scheelite as a function of T, P, pH, and mNaCl. Economic
643   Geology, 95: 143–182.

644 Xie, G.Q., Mao, J.W., Bagas, L., Fu, B., and Zhang, Z.Y. (2019b) Mineralogy and titanite geochronology of
645   the Caojiaba W deposit, Xiangzhong metallogenic province, southern China: Implications for a distal
646   reduced skarn W formation. Mineralium Deposita, 54, 459–472.

647 Xie, G.Q., Mao, J.W., Li, W., Fu, B., and Zhang, Z.Y. (2019a) Granite-related Yangjiashan tungsten deposit,
648   southern China. Mineralium Deposita, 54, 67–80.

649 Yang, J., Bai, D.Y., Wang, X.H., and He, J.N. (2015) Zircon SHRIMP U-Pb dating and geochemistry of
650   Caledonian Baimashan pluton and its tectonic significance. Geology and Mineral Resources of South
651   China, 31, 48–56 (in Chinese with English abstract).

652 Yang, Y.H., Chu, Z.Y., Wu, F.Y., Xie, L.W., and Yang, J.H. (2011) Precise and accurate determination of
653   Sm, Nd concentrations and Nd isotopic compositions in geological samples by MC–ICP–MS. Journal of
654   Analytical Atomic Spectrometry, 26, 1237–1244.

655 Yang, Y.H., Wu, F.Y., Yang, J.H., Chew, D.M., Xie, L.W., Chu, Z.Y., Zhang Y.B., and Huang, C. (2014) Sr
656   and Nd isotopic compositions of apatite reference materials used in U-Th-Pb geochronology. Chemical
657   Geology, 385, 35–55.

658 Zhang, L.S., Peng, J.T., and Lin, F.M. (2020) Mineralogical, geochemical characteristics and formation

659   mechanism of skarn minerals in the Darongxi tungsten deposit, western Hunan. Geological Review, 66,

660   113–138 (in Chinese with English abstract).

661   Zhao, W.W., Zhou, M.F., Williams-Jones, A.E., and Zhao, Z. (2018) Constraints on the uptake of REE by

662   scheelite in the Baoshan tungsten skarn deposit, south China. Chemical Geology, 477, 123–136.

663   Zhu, Y.N., and Peng, J.T. (2015) Infrared microthermometric and noble gas isotope study of fluid inclusions

664   in ore minerals at the Woxi orogenic Au–Sb–W deposit, western Hunan, south China. Ore Geology

665   Reviews, 65, 55–69.

666   **FIGURE CAPTIONS**

667   **FIGURE 1.** Geological map of the Xiangzhong Sb–Au metallogenic province, showing the most important ore

668   deposits and intrusions. Map modified after W. Li et al. (2018).

669   **FIGURE 2.** (**a**) Geological map of the Yangjiashan deposit, and (**b**) representative cross section along

670   exploration line (A–B) showing the occurrence and morphology of the major orebodies of the

671   Yangjiashan deposit (modified after Xie et al. 2019a).

672   **FIGURE 3.** Photographs showing the different stages of tungsten mineralization from the Yangjiashan deposit.

673   (**a, b**) Greisen ores within granite and Banxi Group slate, respectively. (**c, d**) Scheelite-bearing quartz

674   veins within the granite and Banxi Group slate, respectively. Qz−quartz; Sch−scheelite.

675   **FIGURE 4.** Photographs showing the occurrence of two types of ores. **a** and **b** are from the greisen ores; **c** and

676   **d** are from the quartz vein-type ores. (**a, b**) Arsenopyrite, quartz, muscovite coexists with scheelite. (**c**)

677   Sulfides assemblage containing arsenopyrite and pyrite coexists with scheelite, and minor fluorite within

678   the quartz vein. (**d**) Scheelite and coexisting muscovite located at the contact between quartz vein and

679   adjacent silicified slate. (**e**) Scheelite-bearing quartz vein within silicified granite. (**f**) Scheelite coexisting

680   with cassiterite within the quartz vein. (**g**) Coarse-grained scheelite assemblage within the quartz vein. (**h**)

681   Thin veins containing chalcopyrite, pyrite and scheelite within strongly silicified slate. (**i**) Scheelite and

682   coexisting arsenopyrite and pyrite within the quartz vein. Apy−arsenopyrite, Cp−chalcopyrite,

683   Cst−cassiterite, Fl−fluorite, Ms−muscovite, Py−pyrite, Qz−quartz, Sch−scheelite.

684   **FIGURE 5.** Cathodoluminescence (CL) images showing textures features of scheelite from both stages. **a** and

685   **b** are from greisen ores; **c−f** are from quartz vein-type ores. (**a**) Subhedral Sch2 with oscillatory texture

686   overgrowing Sch1. Sch1 displaying weak zonation. (**b**) Euhedral Sch2 with oscillatory texture. (**c**)

687   Textural features of different types of scheelite from Stage 2. Sch3 showing oscillatory texture

688   characterized by bright and dark zones. Sch4 with homogeneous texture overgrowing Sch3. Sch5

29

689   replacing the earlier two types of scheelite. (**d**) Euhedral Sch3 with well-developed oscillatory texture

690   overprinted by patchy Sch4, then both Sch3 and Sch4 overprinted and replaced by Sch5. (**e**) Sch3

691   irregularly overprinted and replaced by Sch4. (**f**) Sch3 with weak oscillatory zoning. Sch−scheelite.

692   **FIGURE 6.** Plots showing variation in the concentration of selected trace elements from the different types of

693   scheelite. See text for additional explanation.

694   **FIGURE 7.** Chondrite-normalized REE fractionation patterns of scheelite from the Yangjiashan deposit. REE

695   data of Baimashan granite from Yang et al. (2015) are shown for comparison.

696   **FIGURE 8.** LA–ICP–MS element maps of representative scheelite including Sch3, Sch4, and Sch5 from Stage

697   2 quartz vein, showing the distribution of REE and other trace elements. Scales in counts-per-second

698   (cps).

699   **FIGURE 9.** LA–ICP–MS element maps of representative Sch3 with oscillatory texture from Stage 2 quartz

700   vein, showing the distribution of REE and other trace elements. Scales in counts-per-second (cps).

701   **FIGURE 10.** Plots showing variation in Sr and Nd isotopes from different types of scheelite. See text for

702   additional explanation.

703   **FIGURE 11.** Representative CL images showing the texture of scheelite and corresponding variations in

704   chondrite-normalized REE fractionation patterns. All grains are from Stage 2.

705   **FIGURE 12.** Plot of $\varepsilon Nd(t)$ vs. $^{87}Sr/^{86}Sr$ showing the features of scheelite. The endmember mixing curve was

706   made assuming the Banxi Group with the highest $^{87}Sr/^{86}Sr$ and lowest εNd values, or the Banxi Group

707   with the highest $^{87}Sr/^{86}Sr$ and εNd values, respectively. The box means the ranges for Sr and Nd isotope

708   compositions.

709   **FIGURE 13.** Plot of chondrite-normalized Eu concentrations (Eu_N) against calculated Eu_N^* values of scheelite

710   from the Yangjiashan deposit. Note that $Eu_N^* = (Sm_N \times Gd_N)^{1/2}$. Dashed line represents δEu ($\delta Eu = Eu_N/$

711   Eu_N^*) values.

<center>**SUPPLEMENTARY MATERIAL**</center>

713   **Supplementary[1]**

714   **TABLE S1.** Description of samples discussed in the present study

715   **TABLE S2.** Average minimum detection limits and dwell times for LA–ICP–MS spot analysis and mapping

716   **TABLE S3.** Laser ablation inductively coupled plasma mass spectrometry trace element data for scheelite

717   from the Yangjiashan deposit (ppm)

718   **TABLE S4.** Complete *in-situ* Sr isotope dataset for scheelite from the Yangjiashan deposit

719   **TABLE S5.** Complete *in-situ* Nd isotope dataset for scheelite from the Yangjiashan deposit

720   **TABLE S6.** Complete dataset of whole rock Sr isotope data for wallrock and granite

721   **TABLE S7.** Complete dataset of whole rock Nd isotope data for wallrock and granite

722   **FIGURE A1.** REE-bearing minerals within scheelite

723   **FIGURE A2.** Vapor-rich and liquid-rich fluid inclusions co-existed within scheelite and quartz from Stage 2

724   **FIGURE A3.** Log $\alpha H_2 S$ versus log fO_2 diagrams showing the fields of stability for sulfides

TABLE 1. LA–ICP–MS data for scheelite from the Yangjiashan deposit (ppm)

Sub-type	1 (n=5)			2 (n=26)			3 (n=162)			4 (n=29)			5 (n=52)		
Stage	1						2								
	Max	Min	Mean	Max	Min	Mean	Max	Min	Mean	Max	Min	Mean	Max	Min	Mean
Na	186	157	169	112	34.9	69.7	300	9.50	75.8	250	8.50	68.3	174	bdl	55.5
Mg	2.70	2.04	2.29	51.9	4.53	17.1	73.6	1.92	15.4	28.5	3.20	8.05	28.1	2.10	13.9
Mn	132	115	124	48.7	24.7	38.3	92.2	11.7	53.6	76.1	24.1	54.9	68.3	0.58	23.7
Sr	116	84.8	94.9	153	48.9	66.5	193	42.2	72.8	118	36.0	70.9	1025	42.3	264
Mo	45.7	41.0	43.9	21.8	6.99	11.8	36.0	4.09	14.5	32.7	3.93	17.8	30.4	bdl	9.02
Nb	19.5	11.8	14.1	732	107	284	561	8.85	176	312	4.54	95.8	300	3.71	70.5
Pb	46.0	41.3	43.5	37.4	20.8	31.8	55.4	11.5	34.5	45.2	12.6	36.1	49.7	0.20	15.2
La	203	137	163	56.1	4.39	21.6	443	2.23	88.6	321	12.8	110	201	0.56	33.3
Ce	494	353	404	187	23.8	81.3	762	14.9	240	700	36.2	255	502	3.86	108
Pr	66.4	51.0	56.3	31.2	5.64	15.5	87.9	4.10	35.2	83.2	3.77	32.2	63.2	1.12	17.4
Nd	248	203	220	157	41.0	86.4	351	21.0	154	323	10.3	129	278	7.69	84.8
Sm	43.2	39.2	40.8	63.3	18.2	38.5	112	4.95	42.5	119	2.07	33.1	78.3	4.19	24.6
Eu	27.1	11.1	17.0	28.1	4.47	14.1	55.3	4.79	20.2	36.6	4.26	18.9	20.1	1.17	7.28
Gd	34.2	28.3	31.7	123	44.7	78.4	151	6.51	54.1	149	1.99	39.5	80.6	8.00	29.4
Tb	5.68	4.36	5.07	26.1	11.2	18.2	31.7	1.21	11.3	26.9	0.39	7.71	16.0	1.50	5.33
Dy	38.5	25.9	31.8	200	95.9	144	232	8.02	87.8	192	2.70	55.5	116	9.20	36.7
Ho	7.86	5.07	6.32	47.3	22.7	34.0	51.0	1.70	20.6	44.4	0.60	12.4	25.9	1.80	8.02
Er	23.6	13.9	17.9	150	70.0	107	159	6.06	67.1	133	2.20	38.6	79.0	3.96	23.9
Tm	3.37	1.86	2.50	21.8	10.0	15.9	22.6	1.39	10.4	16.7	0.45	5.96	11.1	0.37	3.40
Yb	21.5	11.8	16.1	127	63.4	100	165	5.97	70.4	108	4.13	43.4	76.4	1.59	21.6
Lu	2.60	1.44	1.98	15.7	7.63	12.0	24.7	0.63	9.35	13.9	0.64	5.98	10.3	0.16	2.74
Y	219	126	165	1,380	667	1,036	1,420	81.9	724	1,077	29.8	402	779	32.1	242

ΣREE	1,172	938	1,015	1,082	522	767	1,801	184	911	1,609	98.0	788	1,243	51.2	407
LREE	1,066	803	901	508	111	257	1,627	72.6	580	1,485	83.9	579	1,080	21.4	276
HREE	136	92.6	113	681	327	509	747	55.2	331	620	14.0	209	401	29.7	131
LREE/HREE	10.1	5.9	8.1	0.9	0.2	0.5	15.1	0.3	2.6	12.5	0.4	6	6.6	0.5	2.1
δEu	2.2	1.0	1.4	1.6	0.2	0.8	14.7	0.2	2.1	20.7	0.3	5.5	2.5	0.2	0.9

Note: bdl signifies that measured data are below minimum detection limits.

TABLE 2. Measured *in-situ* Sr isotope data for scheelite from the Yangjiashan deposit

Sub-type	Stage			^{85}Rb(v)	^{88}Sr(v)	^{84}Sr/^{86}Sr	2σ	^{87}Rb/^{86}Sr	2σ	^{87}Sr/^{86}Sr	2σ
1	1	n=3	Max	0.00100	0.90	0.05743	0.00180	0.00477	0.00015	0.72396	0.00038
			Min	0.00041	0.65	0.05561	0.00139	0.00206	0.00008	0.71939	0.00035
			Mean	0.00077	0.75	0.05656	0.00154	0.00336	0.00011	0.72166	0.00036
2		n=5	Max	0.00989	0.84	0.05815	0.00420	0.03639	0.00726	0.72617	0.00085
			Min	0.00147	0.31	0.04508	0.00189	0.01262	0.00023	0.71711	0.00047
			Mean	0.00368	0.45	0.05340	0.00328	0.02147	0.00264	0.72326	0.00071
3	2	n=17	Max	0.00324	1.80	0.05699	0.00232	0.01431	0.00164	0.72573	0.00044
			Min	0.00062	0.61	0.05466	0.00082	0.00122	0.00008	0.71898	0.00018
			Mean	0.00160	1.00	0.05588	0.00141	0.00595	0.00046	0.72189	0.00033
4		n=5	Max	0.00166	0.91	0.05806	0.00215	0.00754	0.00020	0.72010	0.00041
			Min	0.00023	0.65	0.05586	0.00149	0.00096	0.00010	0.71906	0.00030
			Mean	0.00082	0.78	0.05654	0.00179	0.00351	0.00015	0.71956	0.00037
5		n=25	Max	0.01447	5.81	0.05858	0.00375	0.02288	0.00451	0.71843	0.00081
			Min	0.00019	0.32	0.05559	0.00021	0.00021	0.00002	0.71336	0.00007
			Mean	0.00182	2.56	0.05619	0.00102	0.00424	0.00064	0.71543	0.00026

Note: (v) means voltages for Rb and Sr isotope measurement

TABLE 3. Measured *in-situ* Nd isotope data for scheelite from the Yangjiashan deposit

Sub-type	Stage			$^{147}Sm/^{144}Nd$	2σ	$^{143}Nd/^{144}Nd$ (0)	2σ	$^{143}Nd/^{144}Nd$ (400)	εNd (400)	2σ
1	1	n=6	Max	0.22990	0.00092	0.51201	0.00005	0.51142	-13.7	1.06
			Min	0.12991	0.00048	0.51169	0.00003	0.51127	-16.7	0.57
			Mean	0.18925	0.00072	0.51184	0.00004	0.51134	-15.3	0.82
2		n=13	Max	0.29343	0.00714	0.51212	0.00010	0.51148	-12.5	1.91
			Min	0.19485	0.00016	0.51188	0.00004	0.51127	-16.7	0.70
			Mean	0.24121	0.00106	0.51199	0.00005	0.51136	-14.9	1.06
3	2	n=52	Max	0.19458	0.00103	0.51209	0.00015	0.51173	-7.7	2.96
			Min	0.09147	0.00007	0.51122	0.00002	0.51085	-24.9	0.49
			Mean	0.14482	0.00036	0.51170	0.00004	0.51132	-15.7	0.82
4		n=6	Max	0.23282	0.00099	0.51170	0.00006	0.51132	-15.7	1.26
			Min	0.09262	0.00024	0.51145	0.00004	0.51099	-22.1	0.72
			Mean	0.16257	0.00043	0.51159	0.00005	0.51117	-18.7	0.92
5		n=5	Max	0.18762	0.00042	0.51182	0.00005	0.51135	-15.2	0.98
			Min	0.16402	0.00018	0.51156	0.00004	0.51112	-19.6	0.86
			Mean	0.17705	0.00029	0.51168	0.00005	0.51122	-17.6	0.90

Note: $^{143}Nd/^{144}Nd$ (400) = $^{143}Nd/^{144}Nd$ (0) - $^{147}Sm/^{144}Nd$ × (Exp (λ_{Sm} × 400 Ma ×1000000) - 1), εNd (400) = (($^{143}Nd/^{144}Nd$ (400) $_{sample}$/$^{143}Nd/^{144}Nd$ $_{CHUR}$) - 1)*10000. The values for λ_{Sm} and $^{143}Nd/^{144}Nd$ $_{CHUR}$ are 6.54×10^{-12} and 0.512638, respectively.
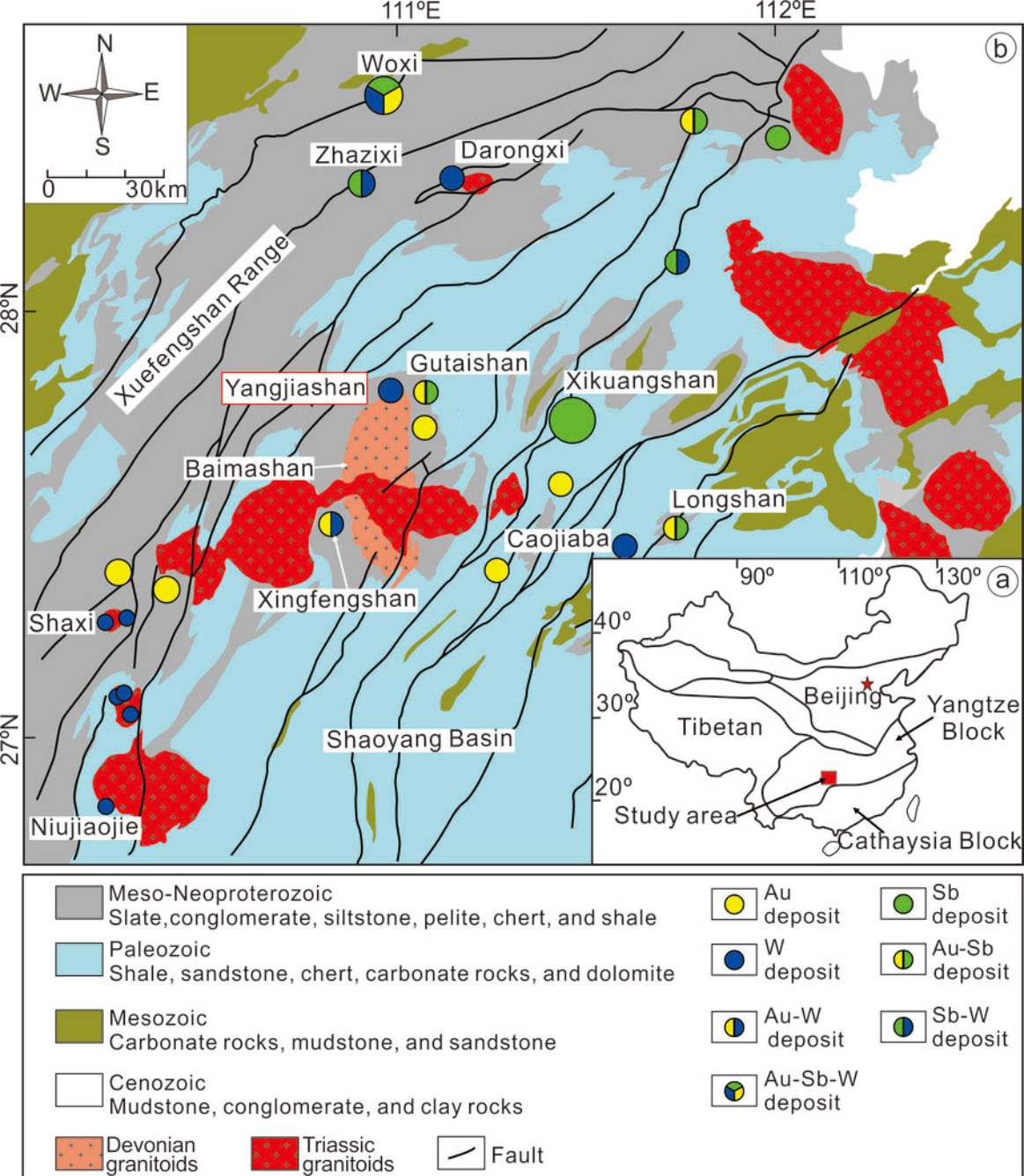
Figure 1
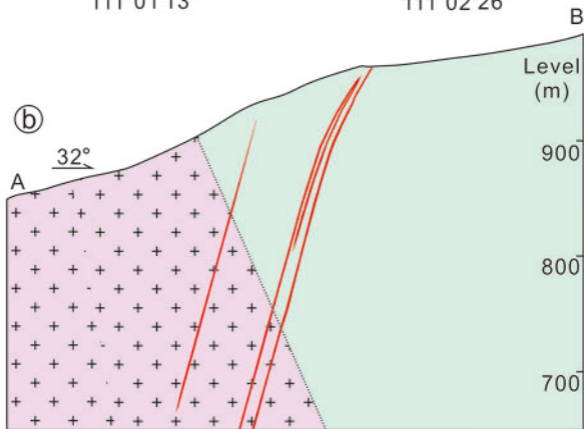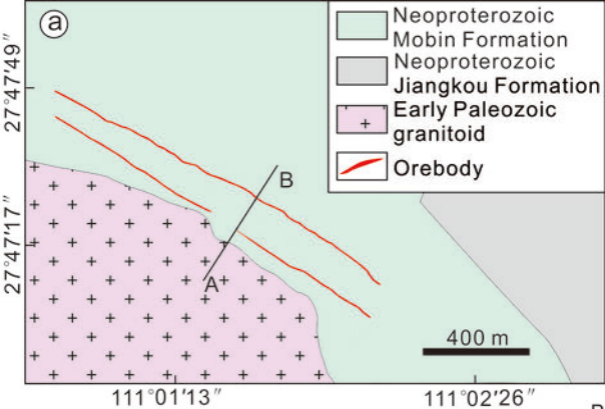
Figure 2
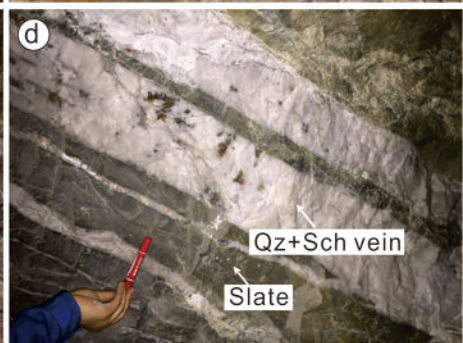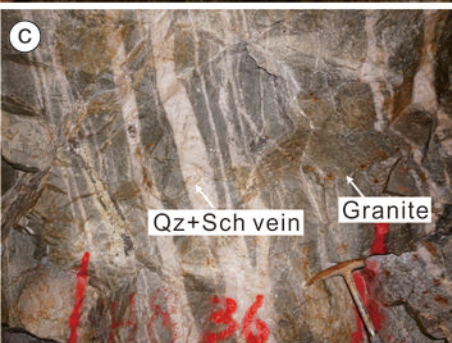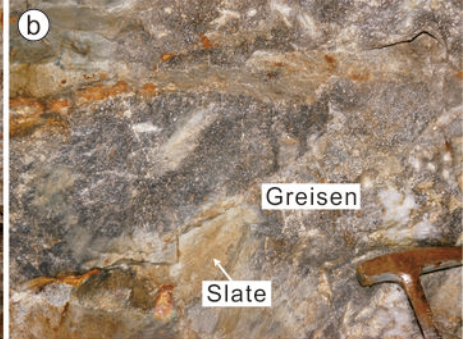
Figure 3
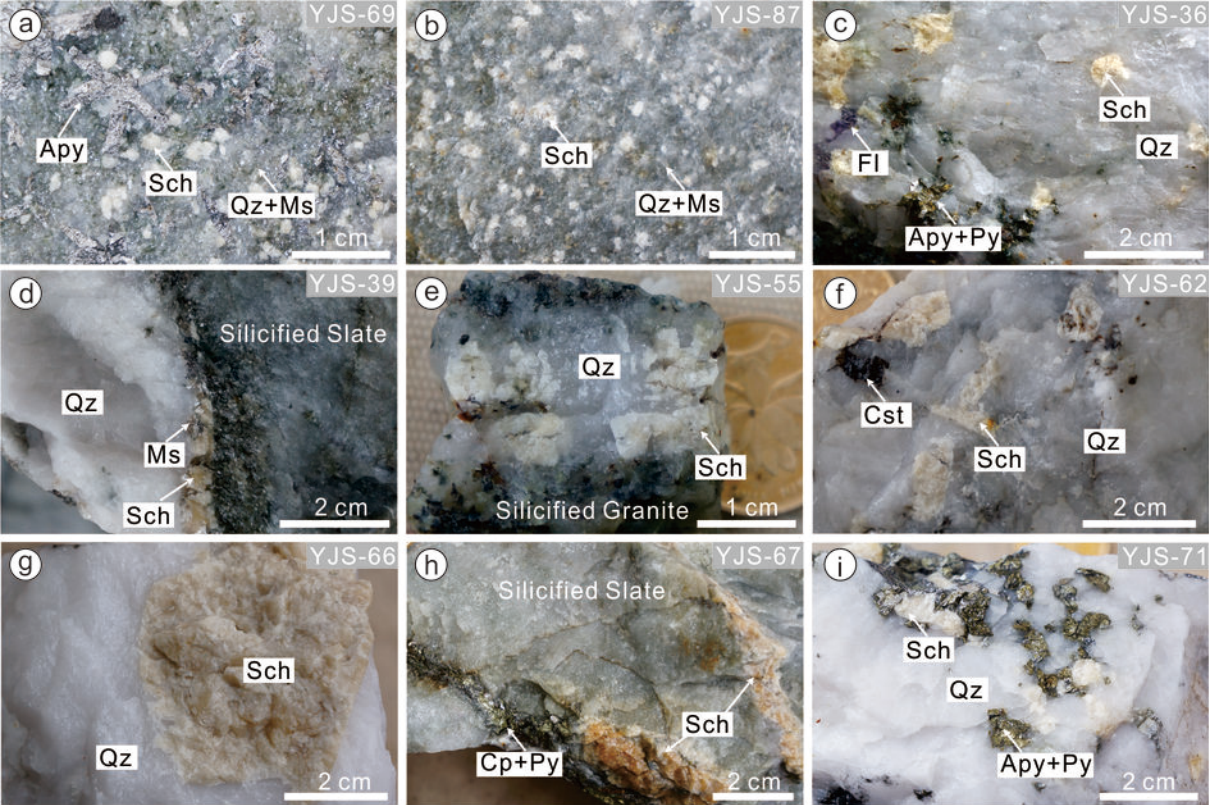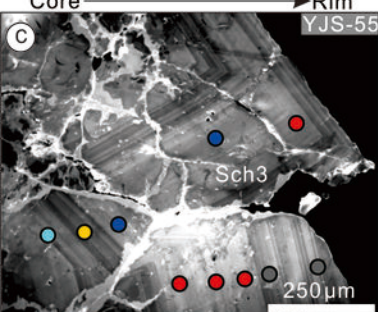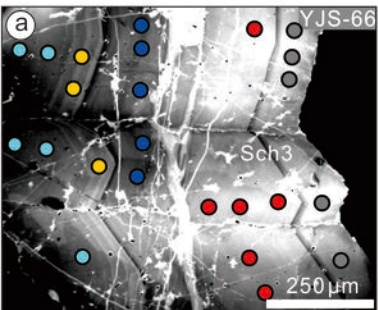
Figure 4
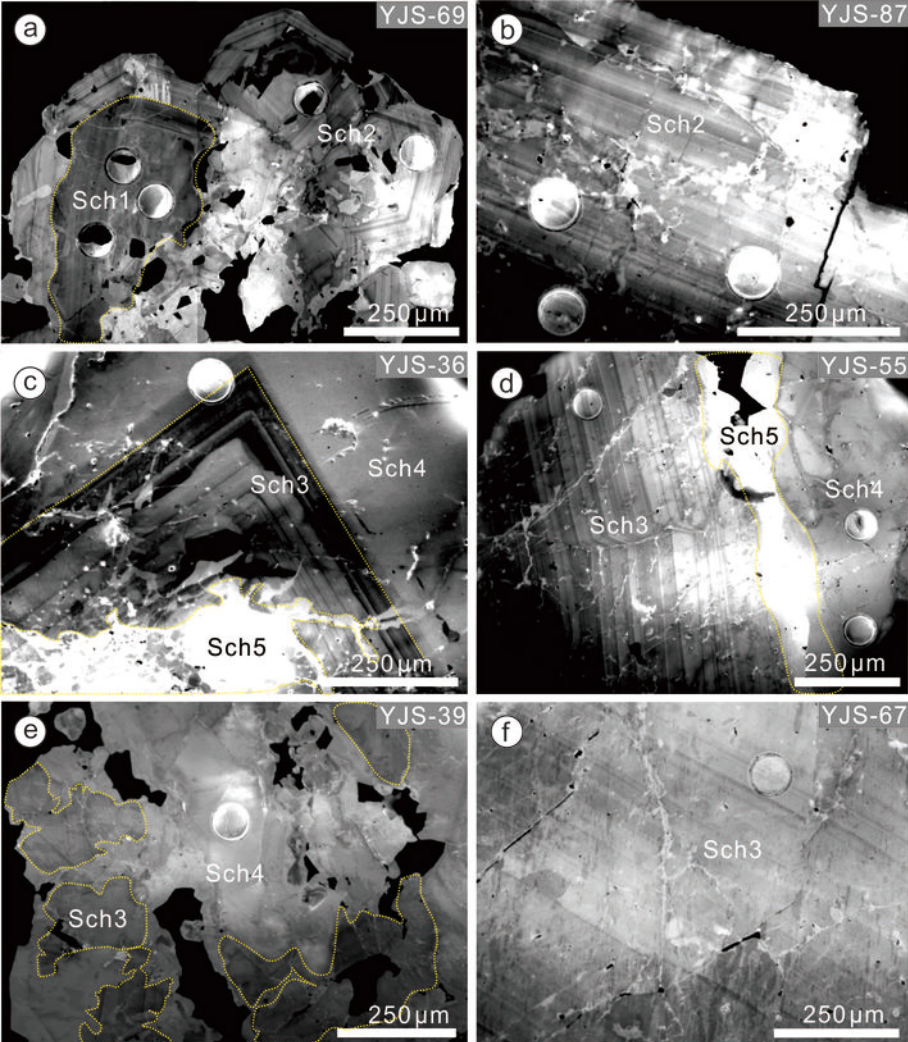
Figure 5
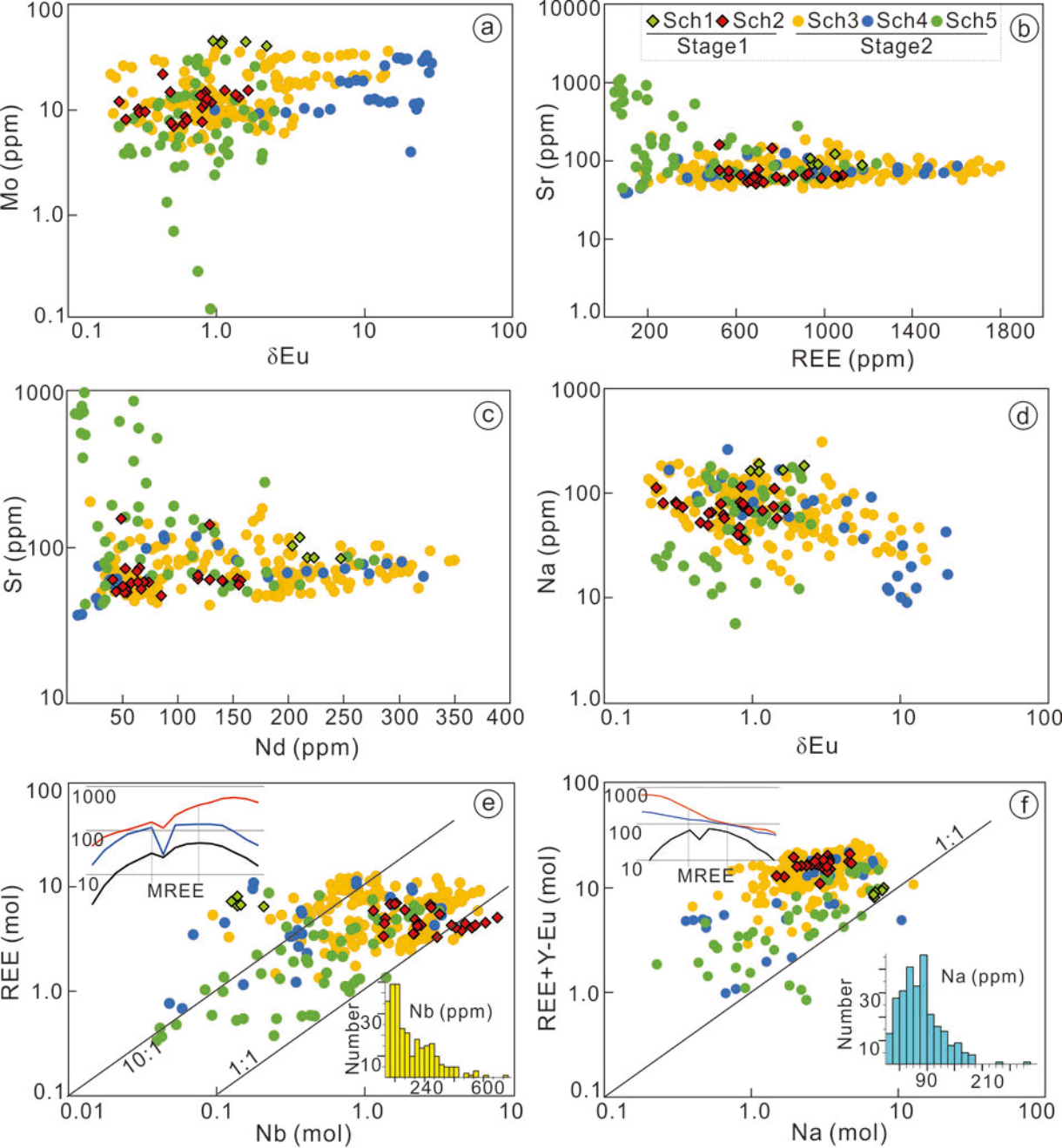
Figure 6
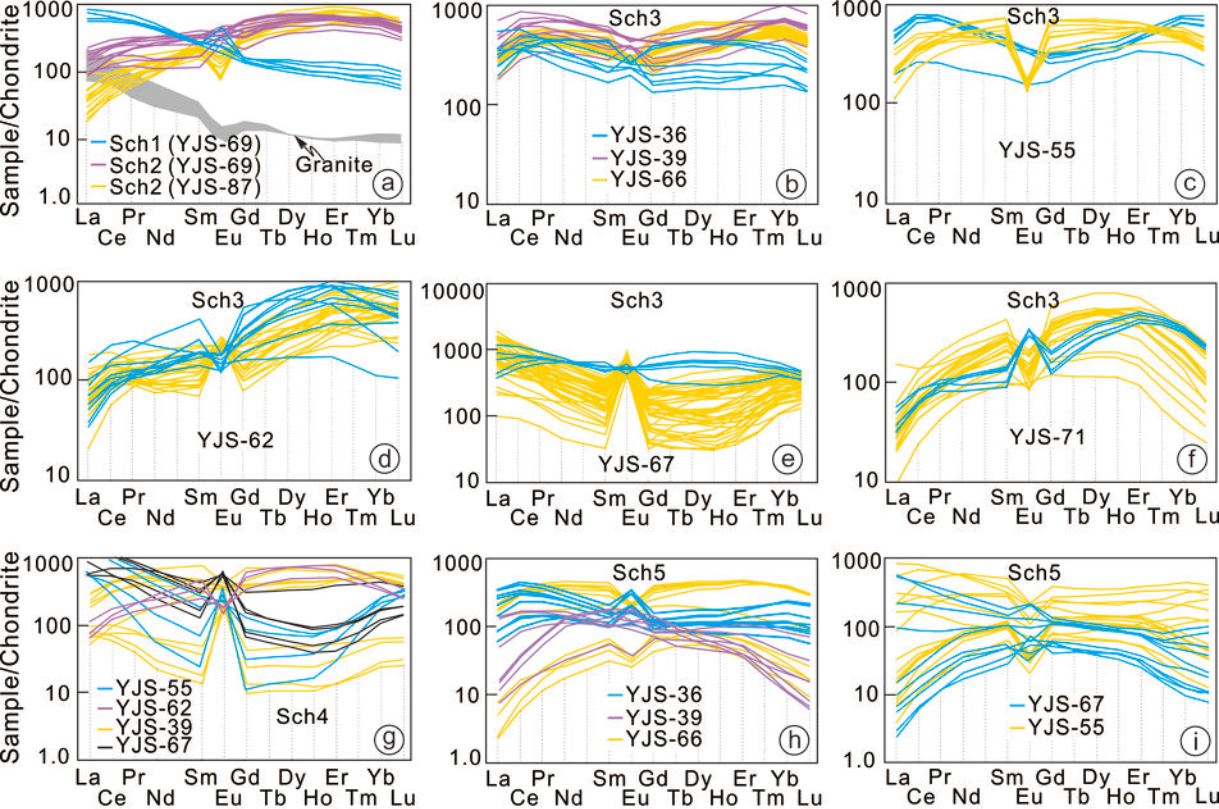
Figure 7
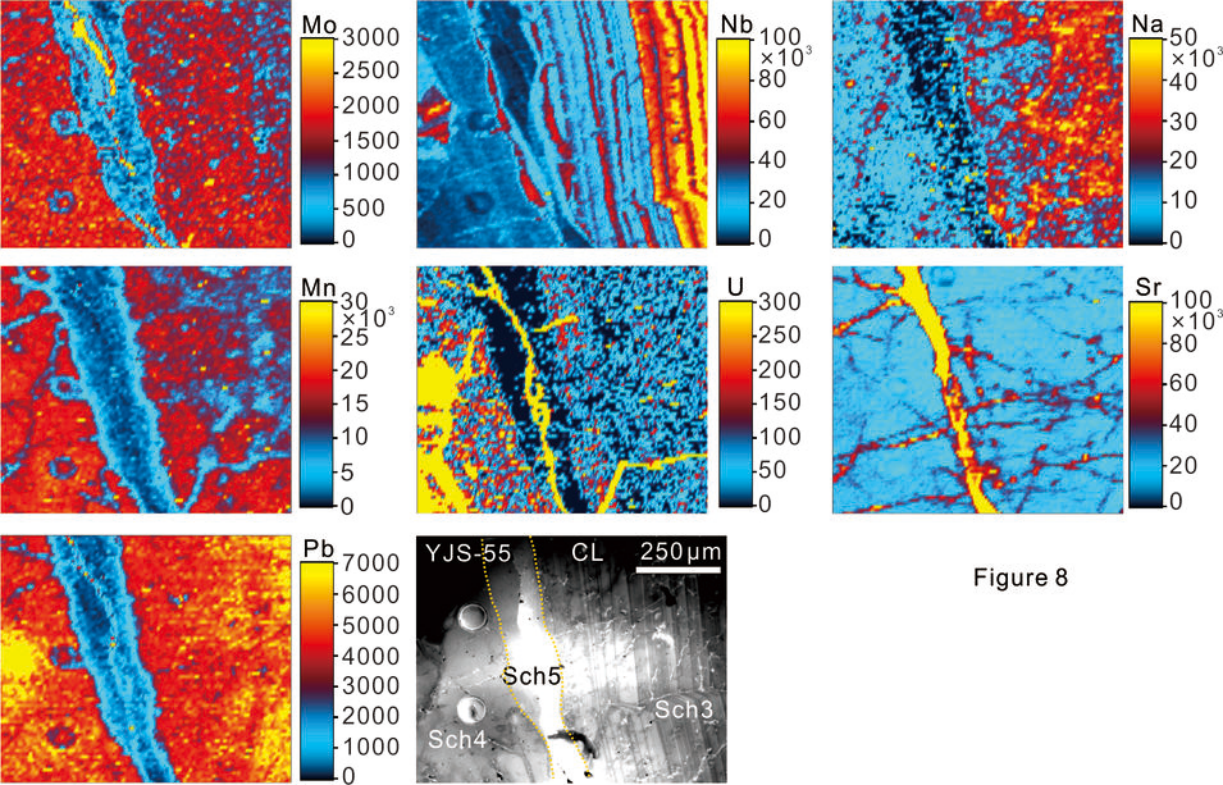
Figure 8
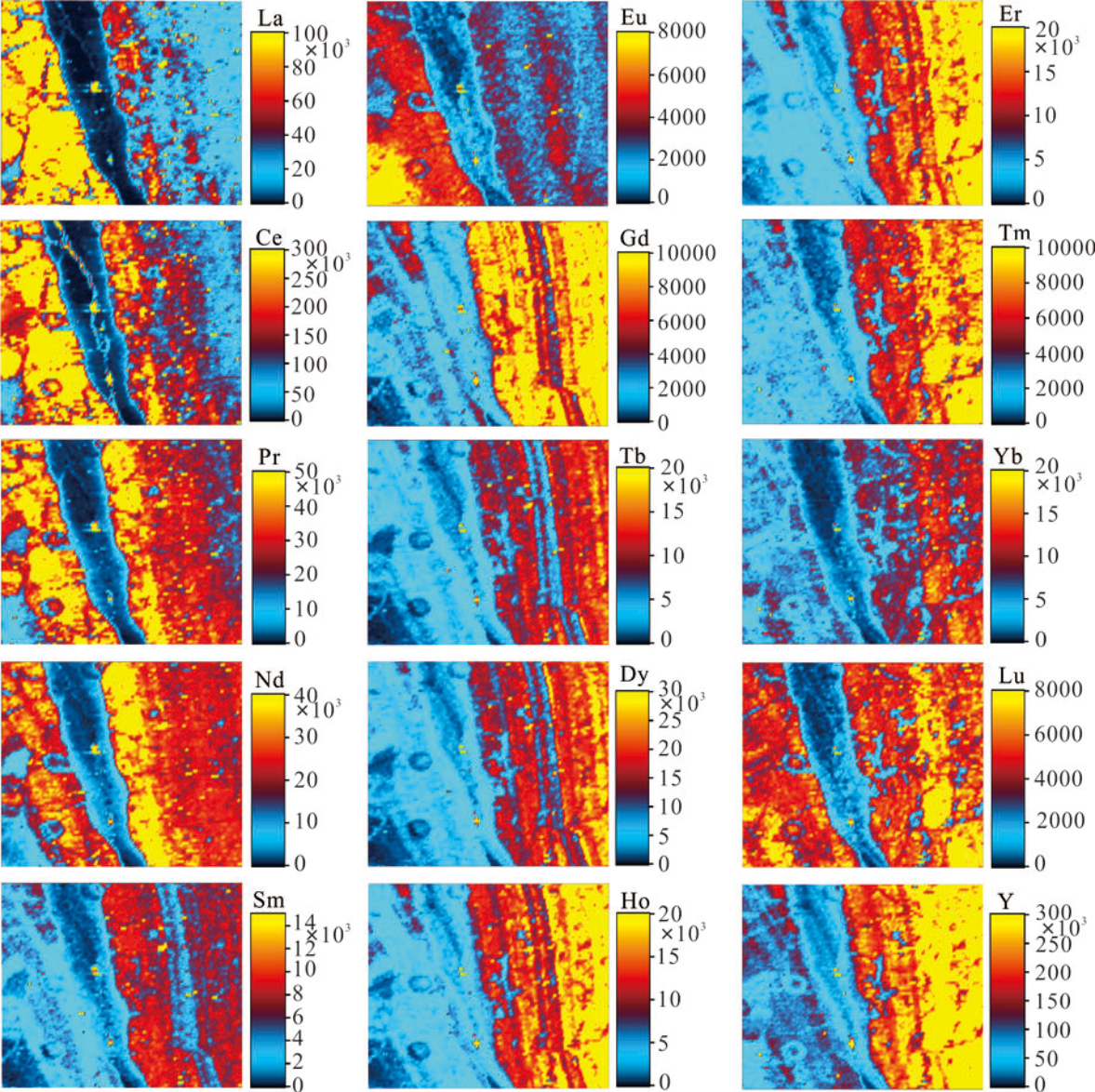
Figure 8
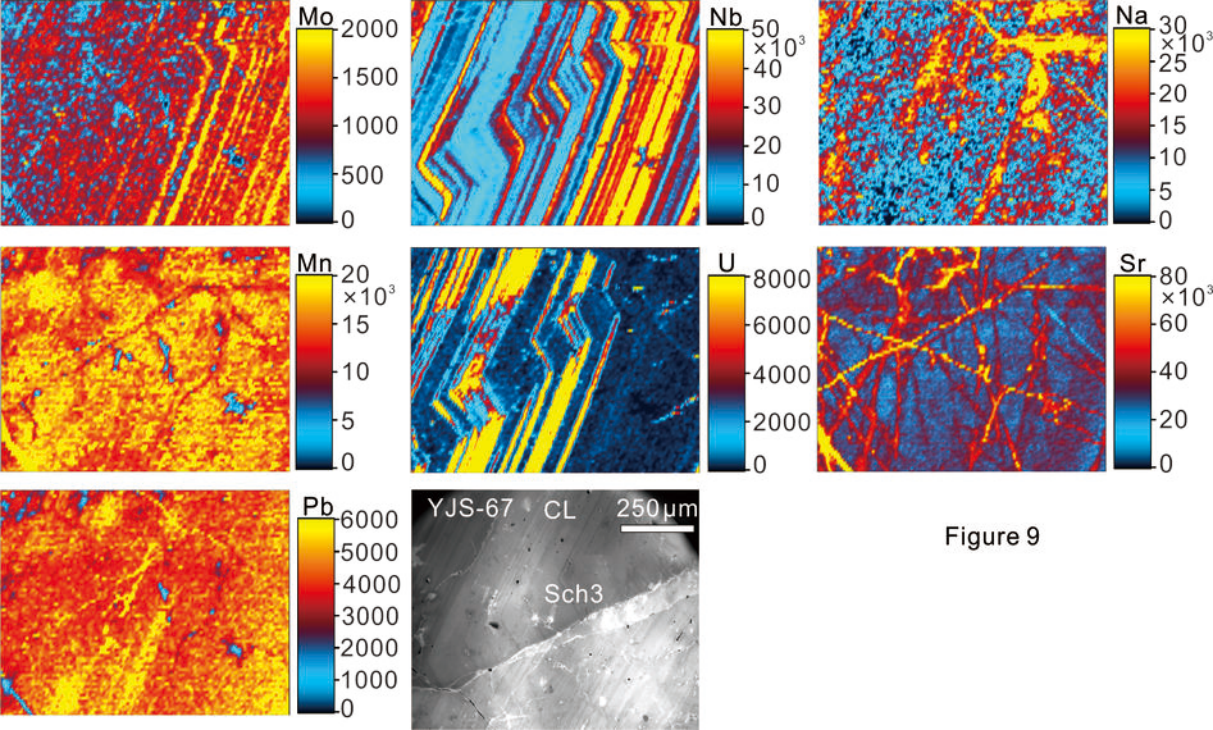
Figure 9
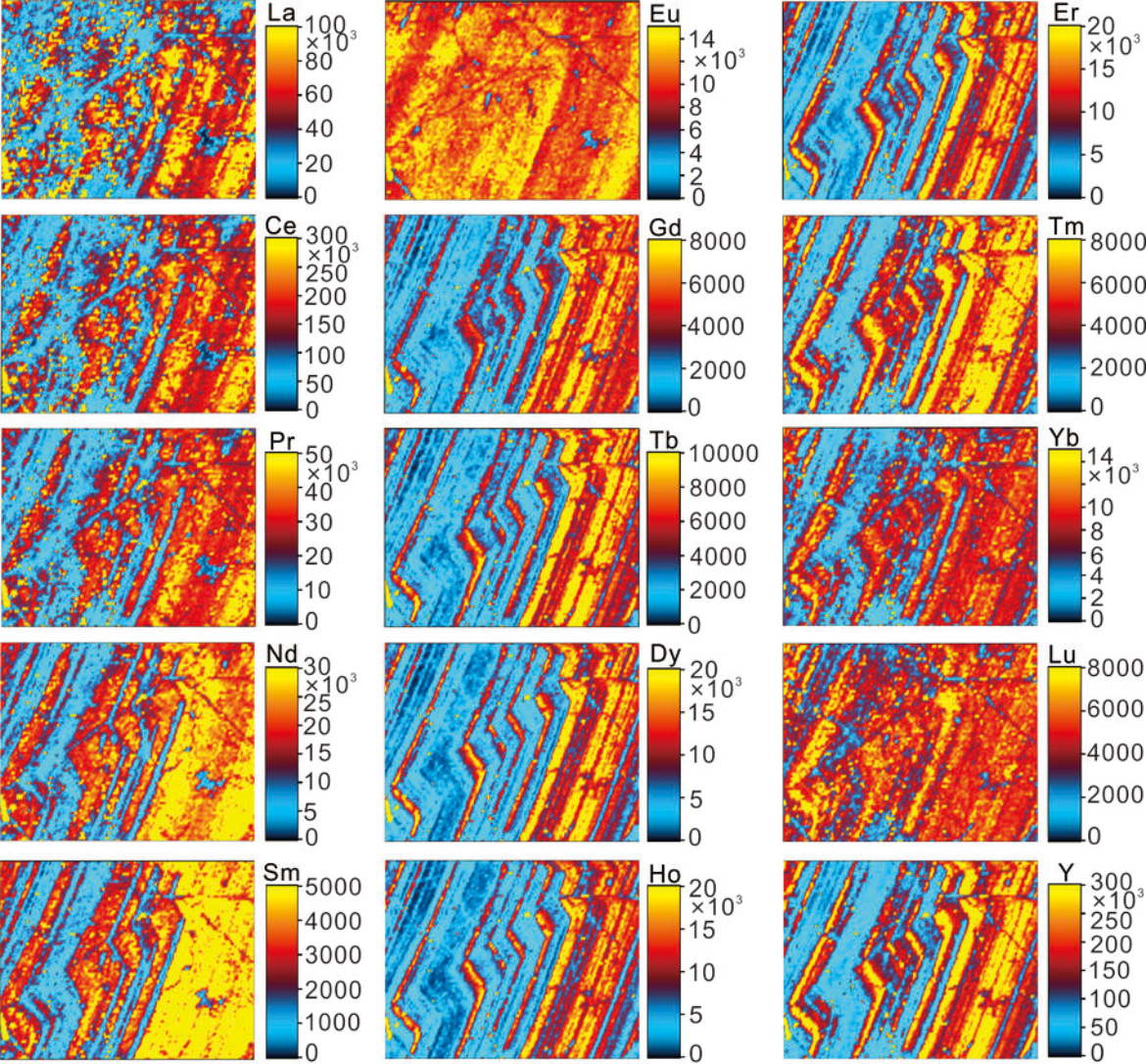
Figure 9
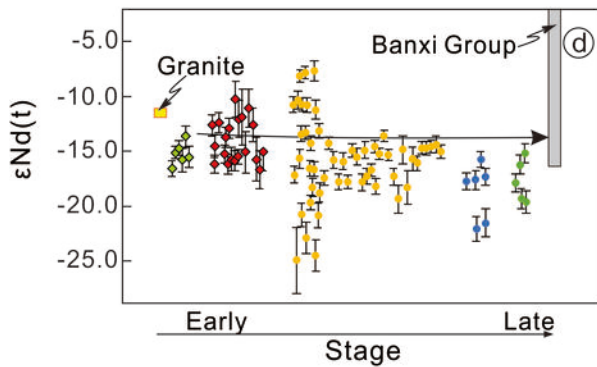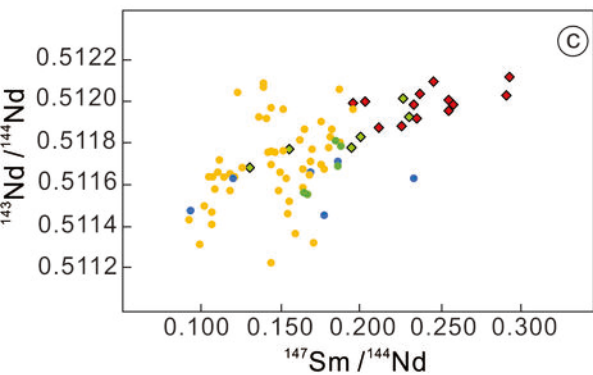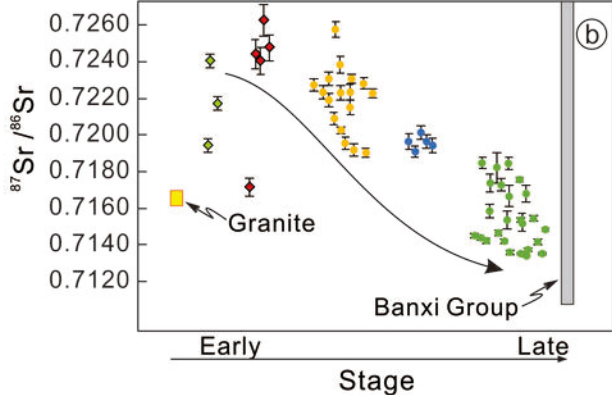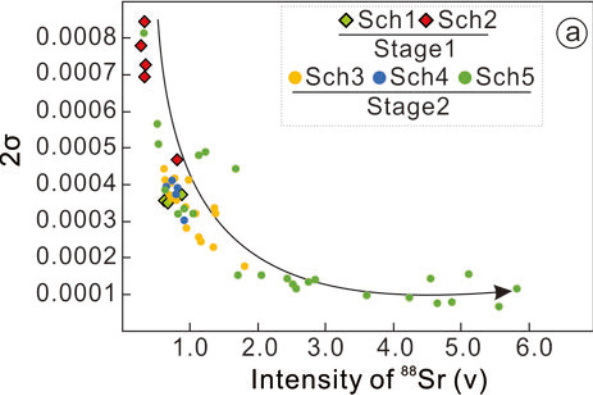
Figure 10
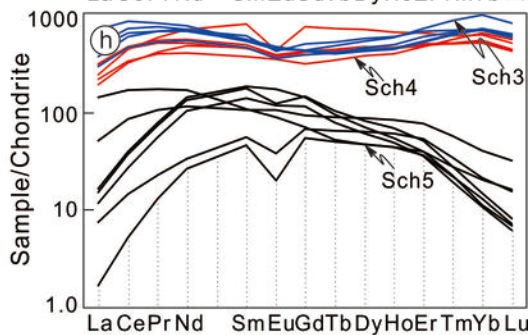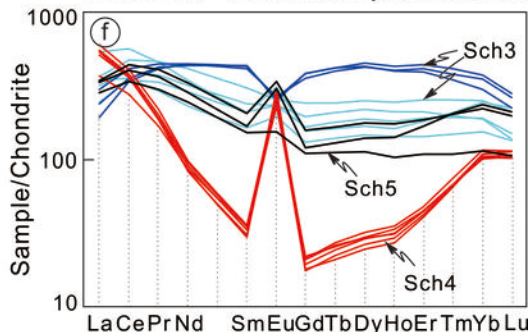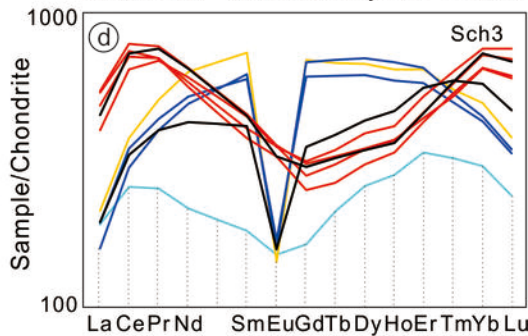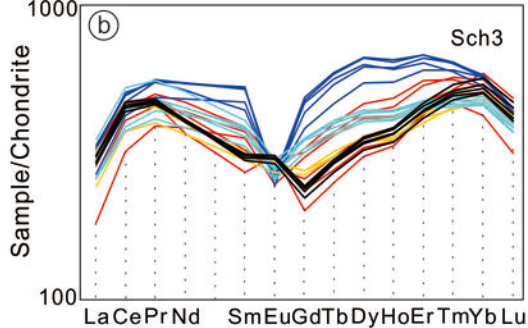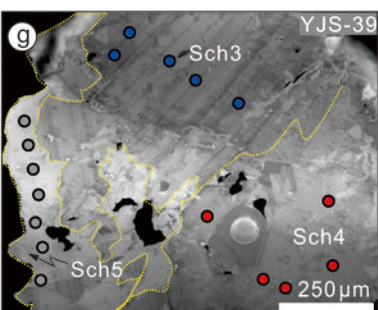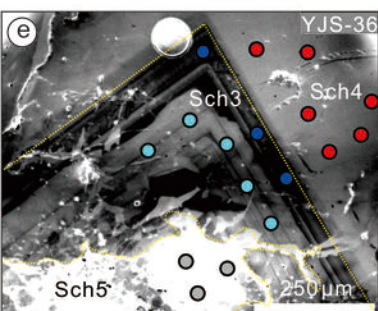
Figure 11

Figure 12

Figure 13